POLITECNICO DI MILANO

School of Industrial and Information Engineering

Master of Science
in
Physics Engineering – Nanophysics and Nanotechnology

Magnetic dynamics of $CaIrO_3$ probed by resonant inelastic x-ray scattering

Supervisor: Prof. Marco MORETTI

Author:

Pietro MARABOTTI
Nr. 883984

Academic Year 2017 - 2018

Politecnico di Milano:
www.polimi.it

School of Industrial and Information Engineering:
www.ingindinf.polimi.it

"We shall not cease from exploration
and the end of all our exploring
will be to arrive where we started
and know the place fo the first time."

T. S. Eliot, *Little Gidding*

Sommario

La presente tesi tratta dell'analisi delle proprietà magnetiche del $CaIrO_3$ mediante l'uso di *resonant inelastic x-ray scattering* (RIXS). Il $CaIrO_3$ appartiene a una nuova classe di materiali fortemente correlati della serie *5d*, chiamati iridati. Negli iridati, ci aspettiamo che la correlazione elettronica sia debole, mentre l'accoppiamento spin-orbita (SOC) risulta avere un effetto importante tanto da modificare la struttura elettronica di questi composti, generando il cosiddetto $j_{eff} = 1/2$ *Mott insulating state*. La struttura cristallina del $CaIrO_3$ è caratterizzata da ottaedri IrO_6 connessi tra loro condividendo sia i vertici che i lati lungo gli assi c e a rispettivamente, a cui la teoria associa interazioni magnetiche di diversa origine e forza. Inoltre, la forte distorsione tetragonale, la cui scala di energia è comparabile con quella del SOC, modifica la struttura elettronica dello stato $j_{eff} = 1/2$ e potrebbe introdurre anisotropie negli accoppiamenti magnetici. Misurando con il RIXS al lato di assorbimento L_3 dell'iridio, siamo in grado di sondare le proprietà magnetiche ed elettroniche del $CaIrO_3$ grazie alla buona risoluzione in energia e ad una sezione d'urto favorevole.

Ho effettuato gli esperimenti RIXS presso la beamline ID20 dell'European Synchrotron Radiation Facility (ESRF). I dati RIXS mostrano una dipendenza in temperatura fortemente correlata con la temperatura di Néel del sistema. Inoltre, la dipendenza dal momento trasferito mostra una forte modulazione dell'intensità e della forma degli spettri RIXS lungo l'asse c. Riferendomi alla letteratura, ho concluso che la dinamica delle eccitazioni a bassa energia del $CaIrO_3$ è dominata da eccitazioni *two-spinon*, da cui deduco che il magnetismo di questo sistema ha un carattere prevalentemente monodimensionale. Ho adottato il modello 1D della catena di spin di tipo Heisenberg con $s = 1/2$ per estrarre le interazioni magnetiche rilevanti nel $CaIrO_3$. Per fare ciò, ho simulato e comparato il fattore di struttura dinamico per le catene magnetiche accoppiate con i dati sperimentali. Ho ottenuto così alcuni valori per gli accoppiamenti magnetici i quali risultano consistenti con la letteratura.

Abstract

In this thesis, I focus on the investigation of $CaIrO_3$ by means of resonant inelastic x-ray scattering (RIXS). $CaIrO_3$ belongs to a new class of strongly correlated electron materials of the *5d* series, namely iridates. In iridates, the electron correlation is expected to be weak, whereas spin-orbit coupling (SOC) is strong and alters the electronic structure of these compounds, leading to the so-called $j_{eff} = 1/2$ Mott insulating state. The crystal structure of $CaIrO_3$ features both corner- and edge-sharing IrO_6 octahedra along the c and a axes, respectively, which are theoretically predicted to support magnetic couplings of different strength and nature. Furthermore, the strong tetragonal distortion, whose energy scale is comparable to that of SOC, modifies the electronic structure of the $j_{eff} = 1/2$ model and possibly introduces anisotropies in magnetic interactions of $CaIrO_3$. Using iridium L_3 edge RIXS, we are able to probe magnetic and electronic properties of $CaIrO_3$ in view of the good energy resolution and the favorable cross section.

I performed RIXS measurements at the ID20 beamline of the European Synchrotron Radiation Facility (ESRF). RIXS data show a characteristic temperature dependence, strongly correlated with the Néel temperature of the system. In addition, the momentum transfer dependence is very peculiar, with strong intensity and modulation of the shape of the RIXS spectra along the corner-sharing direction. By comparison with literature, I conclude that the low-energy dynamics of $CaIrO_3$ is dominated by a two-spinon continuum, thus suggesting that the magnetism in this system has mostly one-dimensional character. I adopt a simple model based on the 1D $s = 1/2$ Heisenberg chain to extract the relevant magnetic interactions in $CaIrO_3$. In order to do so, I compute, calculate and compare the magnetic dynamic structure factor of a coupled spin chain to experimental data. I obtain values of the magnetic couplings which are consistent with that of literature.

Contents

List of Figures

Introduction

The interest over the last decades on the transition metal oxides (TMOs), in particular on the *3d* and *5d* series, is raised due to discovering of some important properties of these strongly correlated electron systems, such as superconductivity in copper oxides (cuprates)[2], colossal magnetoresistance in manganese oxides[3] and multiferroicity[4]. The scientific community has mainly focused its attention on the *3d* TMOs, in which the electron correlation is strong, usually modeled using the so-called ($s = 1/2$) Mott insulating state. Instead, *5d* oxides possess a strong spin-orbit coupling (SOC) and a weak electron correlation, due to the large spatial extension of the *5d* orbitals. However, study of Kim et al.[5] demonstrated that the joint action of the electron correlation and the SOC leads to a manifold of unexpected effects, represented in the phase space in Figure 1[1]. The left-hand region is related to Mott insulators and simple metals, which includes *3d* TMOs (cuprates). Our interest focuses on the right-hand part characterized by high values of SOC. The latter is divided into two main groups: topological insulators (or semi-metals) and spin-orbit coupled Mott insulators. A large number of iridates belongs to the latter group, where the combined action of the crystal field, the electron correlation and the SOC yields to the so-called $j_{eff} = 1/2$ Mott insulating

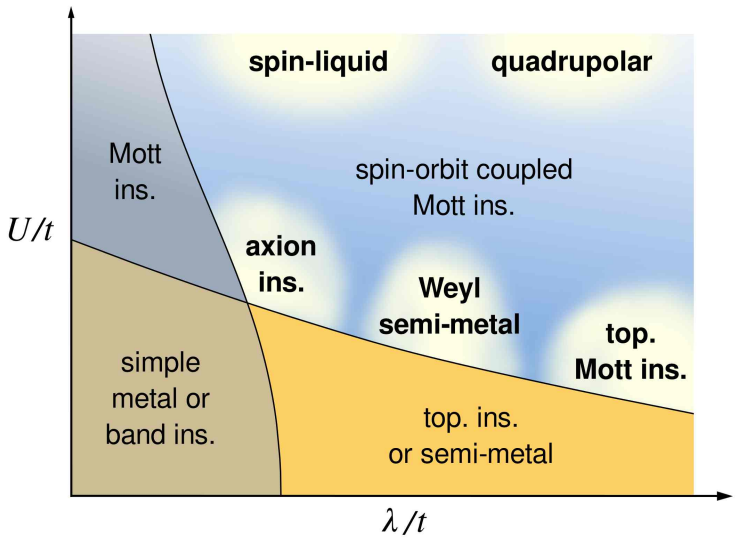

Figure 1: Generic phase diagram of transition metal oxides generated by the joint action of electron correlation and SOC. [Figure taken from Witczak-Krempa et al.[1]].

state[5]. This theory was first invoked by Kim et al.[5] to explain the unexpected insulating character of Sr_2IrO_4 and then extended to many other iridates. The magnetism of the $j_{eff} = 1/2$ Mott insulators is heavily affected by their bond geometry, leading to possible unconventional superconductivity[6] and frustrated magnetism[7]. In Chapter 1, I will shortly review the low-energy physics of iridates, describing the $j_{eff} = 1/2$ Mott insulating model and some important milestones in the investigation of magnetic and electronic properties of iridates. I will particularly focus on $CaIrO_3$: it features a peculiar geometry made by corner- and edge-sharing IrO_6 octahedra[8,9]. Furthermore, $CaIrO_3$ is characterized by a large tetragonal distortion that leads to some modification of the classic $j_{eff} = 1/2$ model[10].

In Chapter 2, I will briefly present resonant inelastic x-ray scattering (RIXS), the technique that will be used in my thesis to probe magnetic dynamics of $CaIrO_3$. Indeed, RIXS is one of the spectroscopic techniques used to investigate iridates magnetic and electronic properties. The energy and momentum resolution of up to date RIXS spectrometers is sufficient to analyze the magnetic and electronic excitations in iridates. In Chapter 2, I will also describe the optical layout and the spectrometer of ID20 beamline at the European Synchrotron Radiation Facility (ESRF) where I carried out my experiments. Finally, I will introduce the finite momentum transfer resolution of the ID20 spectrometer, analyzed in the recent work of Moretti Sala et al.[11], that will be used in the following.

In the first part of Chapter 3 (see Section 3.2), I will report the temperature evolution of low-energy excitations $CaIrO_3$ probed by RIXS. A peculiar trend of the spectral weight in the elastic energy range is found, suggesting a possible magnetic origin of such feature. The second part of Chapter 3 (see Section 3.3) presents the momentum dependence of low-energy excitations, showing a spinon-like dispersion that suggests us a potential one-dimensional spins chain character. However, an actual coupling among chains may have to be considered to take into account the tiny dispersion along the edge-sharing direction. The last part of Chapter 3 (see Section 3.4) is entirely devoted to the description of a model for the two-spin dynamic structure factor for coupled chains, which should reproduce the experimental data. From this model, I will extract numerical values of magnetic couplings along the corner- and edge-sharing direction and I will try to simulate the magnetic dynamics of $CaIrO_3$ (see Section 3.6).

Chapter 1

Physics of iridate compounds

Iridium oxides (iridates) are a class of correlated materials which show some interesting features, such as novel quantum phases or excitations induced by spin-orbit coupling.
In this Chapter, I review the low-energy physics of these fascinating compounds, focusing on calcium iridate, $CaIrO_3$.

1.1 Transition-metal oxides (TMOs) with strong spin-orbit coupling

Transition-metal oxides are very interesting compounds because they display a large class of peculiar phenomena, such as high-temperature superconductivity[2], colossal magneto-resistance[3] and multiferroicity[4]. Great success has been achieved in the study of *3d* transition-metal oxides (TMOs), in which localized *3d* states yield strongly correlated narrow bands with a large on-site Coulomb repulsion U and a small bandwidth W[2–4]. In contrast, *4d* and *5d* orbitals have a larger spatial extension and correlation effects are rather moderate due to a wider bandwidth and a weaker Coulomb repulsion ($U \approx W$)[12]. Such weakening is expected to induce metallic behavior in *4d* and *5d* compounds[13].

The observation of anomalous insulating character in some of the *5d* transition metal oxides (among which, for example, Sr_2IrO_4[14], $Sr_3Ir_2O_7$[15], Na_2IrO_3[16], $CaIrO_3$[8], $NaOsO_3$[17] and $Ca_2Os_2O_7$[18]) has been explained in the work of Kim *et al.*[5], who observed that the large spatial extent of *5d* orbitals is accompanied by a strong spin-orbit coupling (SOC).

The SOC is a relativistic effect due to the interaction between the spin of the electron and its motion[19]. In the electron frame, the orbital motion of the charged nucleus sets up a magnetic field proportional to the angular momentum $\mathbf{l}$ of the electron. The spin-orbit Hamiltonian can be calculated by evaluating the interaction between such field and the magnetic moment of the electron (proportional to the spin angular momentum $\mathbf{s}$) and it is equal to

$$\mathcal{H}_{SOC} = \frac{e^2}{8\pi\varepsilon_0 m^2 c^2}\frac{Z}{r^3}\mathbf{l}\cdot\mathbf{s}, \tag{1.1}$$

where Z is the atomic number and r is the orbital radius. It can be shown that the

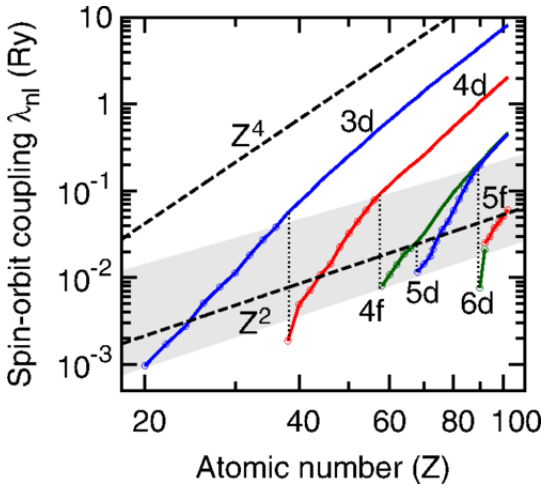

Figure 1.1: Dependence of the SOC strength as a function of the atomic number Z. The Z^4 trend (dashed black line) for *3d* series is compared to Hartree-Fock calculations (colored lines), where for the *outermost* electrons (indicated with circles) the SOC interactions increases more slowly, following a Z^2 trend. [Figure taken from Shanavas et al.[20]].

expectation value $\langle 1/r^3 \rangle$ is proportional to $\langle Z/n \rangle^3$, from which we obtain a scaling factor of Z^4/n^3[19]. It must be noted that the Z^4 proportionality is good when we are considering hydrogen-like wave functions[19]. When we move towards heavier atoms, considering only outer electrons, the SOC constant increases more slowly, following a Z^2 scaling, passing from a shell nd to the following $(n+1)d$ shell[20], as it is shown in Figure 1.1. From calculations, the SOC strength is estimated to be of the order of ~ 50 meV for *3d* compounds and of the order of ~ 0.5 eV for *5d* compounds.

1.2 The $j_{eff} = 1/2$ Mott insulating state in iridates

In iridates, the large crystal field and the SOC modify the bandwidth of *5d* states and, together with electron correlation, induce an insulating state, as shown below[5].

We will use a local model, considering only one iridium ion within its local environment[5]. In most iridates, iridium ion is tetravalent, Ir^{+4}, surrounded by oxygen anions in a octahedral package. Let us first consider the strongest interaction, that is the cubic crystal field[5,21], which splits *5d* levels by ~ 10 Dq (~ 3 eV) into e_g and t_{2g} orbitals[22]. Due to this large splitting, low-spin d^5 electrons occupy t_{2g} levels, with a hole resident in the t_{2g} manifold of $|xy\rangle$, $|xz\rangle$, $|yz\rangle$ orbitals, which has an effective angular moment $l = 1$[23]. It is convenient to express the t_{2g} states as[23]

$$\begin{aligned} \left|t_{2g}^{0}\right\rangle &= |xy\rangle \\ \left|t_{2g}^{+1}\right\rangle &= -\frac{1}{\sqrt{2}}\left(i\,|xz\rangle + |yz\rangle\right) \\ \left|t_{2g}^{-1}\right\rangle &= -\frac{1}{\sqrt{2}}\left(i\,|xz\rangle - |yz\rangle\right) \end{aligned} \tag{1.2}$$

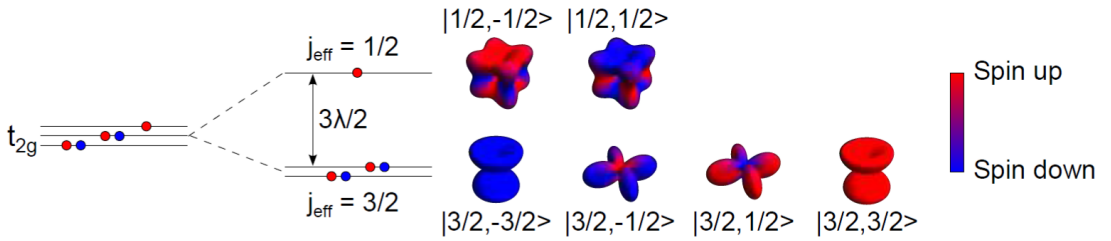

Figure 1.2: Splitting of the t_{2g} orbital into a filled lower-energy $j_{eff} = 3/2$ and an half-filled higher-energy $j_{eff} = 1/2$ orbitals due to the action of the SOC. The electron and the spin densities are also shown for the special case $\Delta = 0$. [Figure taken from Rossi[24]].

Let us now include the effect of the SOC and the effect of octahedral irregularities, such as tetragonal crystal field, that modify the Hamiltonian[23]:

$$\mathcal{H}_0 = \lambda \mathbf{l} \cdot \mathbf{s} + \Delta l_z^2, \tag{1.3}$$

where λ is the SOC constant and Δ represents the strength of tetragonal distortion, i.e. $\Delta > 0$ for elongation or $\Delta < 0$ for compression of the octahedron[38].

The lowest energy level of $\mathcal{H}_0$ is a Kramer's doublet of isospin states[23]:

$$\begin{aligned} \left|\frac{1}{2}, -\frac{1}{2}\right\rangle &= \sin\vartheta \left|t_{2g}^{0}, \uparrow\right\rangle - \cos\vartheta \left|t_{2g}^{+1}, \downarrow\right\rangle \\ \left|\frac{1}{2}, \frac{1}{2}\right\rangle &= \sin\vartheta \left|t_{2g}^{0}, \downarrow\right\rangle - \cos\vartheta \left|t_{2g}^{-1}, \uparrow\right\rangle, \end{aligned} \tag{1.4}$$

where ϑ parameterizes the relative strength of the tetragonal distortion with respect to the SOC, $\tan(2\vartheta) = 2\sqrt{2}\lambda/(\lambda - 2\Delta)$. The energy diagram in $\Delta = 0$ case is reported in Figure 1.2. The t_{2g} manifold is split into a full lower-energy $j_{eff} = 3/2$ quartet and a singly-occupied higher-energy $j_{eff} = 1/2$ doublet. These two bands are separated by an energy of $3\lambda/2$. Figure 1.2 also shows the electron and the spin density wave functions in the case $\Delta = 0$. Their dependence on the relative strength of the tetragonal crystal field Δ and of the SOC λ is reported in Figure 1.3. As can be seen, when $\Delta/\lambda \gg 1$, corresponding to the case of strong octahedral elongation, the $j_{eff} = 1/2$ state is dominated by $\left|t_{2g}^{0}\right\rangle$ orbital (or $|xy\rangle$), and the $j_{eff} = 3/2$ states are mainly formed by $\left|t_{2g}^{\pm 1}\right\rangle$. In the opposite situation, when $\Delta/\lambda \ll -1$, i.e. strong octahedral compression, the ground state possesses mainly $\left|t_{2g}^{\pm 1}\right\rangle$ character, and $\left|\frac{3}{2}, \pm\frac{1}{2}\right\rangle$ states have a dominant $\left|t_{2g}^{0}\right\rangle$ distribution. We note that $\left|\frac{3}{2}, \pm\frac{3}{2}\right\rangle$ wave functions are independent on λ and Δ[24].

The previous discussion can be extended to interacting ions in a crystal, considering electronic bands instead of atomic energy levels. This schematic model refers to Figure 1.4. The partial filling of t_{2g} levels should lead to a metallic behavior of iridates (Figure 1.4(a)). A $s = 1/2$ Mott insulating state could, in principle, be generated assuming a large Coulomb repulsion[5] ($U \gg W$), splitting the t_{2g} band into a filled lower-energy and empty higher-energy sub-bands (Figure 1.4(b)). However, realistic values of U are comparable to W and cannot lead to insulating state[5]. In a strong SOC picture, instead, the t_{2g} band splits into a filled $j_{eff} = 3/2$-derived and

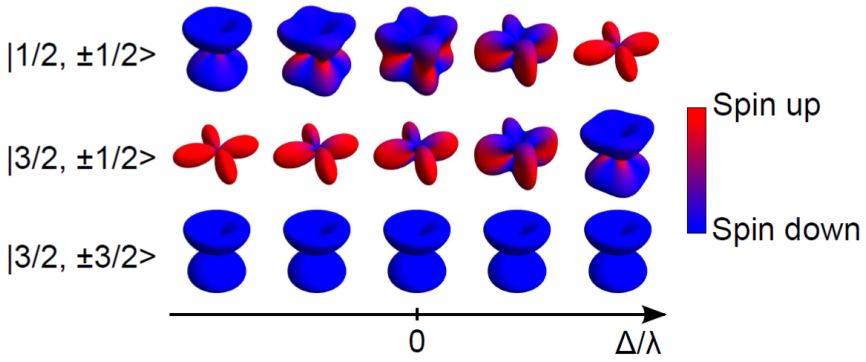

Figure 1.3: Dependence of the electronic and the spin wave functions on the relative strength of the tetragonal crystal filed (Δ) and the SOC (λ). [Figure taken from Rossi[24]].

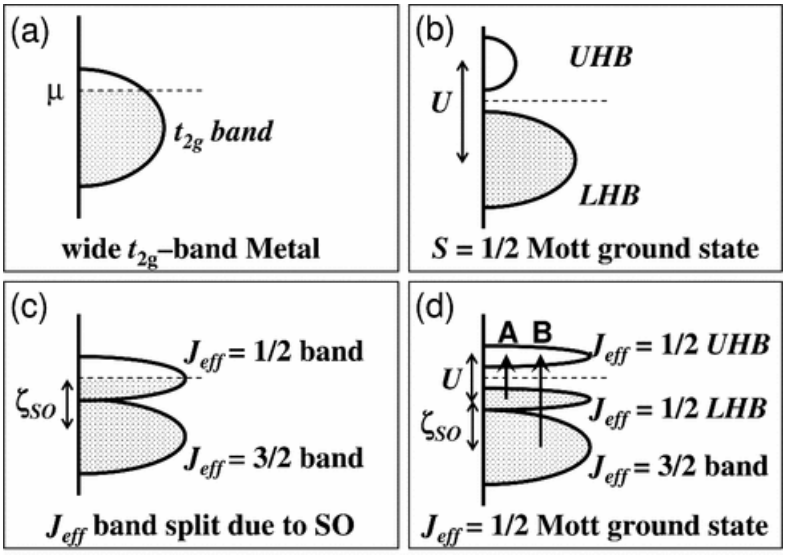

Figure 1.4: Schematic energy diagram of the outermost t_{2g} band configuration (a) without SOC and U, (b) without SOC and with an unrealistically large U, (c) with SOC (ζ_{SO}) but without U, and (d) with SOC and U. [Figure taken from Kim et al.[5]].

an empty $j_{eff} = 1/2$-derived sub-bands (Figure 1.4(c)). The large SOC effectively reduces the bandwidth of the half-filled $j_{eff} = 1/2$ band so that even a moderate Coulomb repulsion can open a gap, leading to the realization of the $j_{eff} = 1/2$ Mott insulating state (Figure 1.4(d))[5].

The first experimental evidence of the existence of the $j_{eff} = 1/2$ ground state has been achieved on Sr_2IrO_4[5]. In Sr_2IrO_4, angle-resolved photoemission spectroscopy (ARPES) (Figure 1.5(a)) and optical conductivity measurements (Figure 1.5(b)) confirm the insulating state and are consistent with the description of the band structure in terms of the $j_{eff} = 1/2$ ground state. In particular, the sharp peak A of Figure 1.5(b) represents the transition from the $j_{eff} = 1/2$ lower Hubbard band (*LHB*) to the $j_{eff} = 1/2$ upper Hubbard band (*UHB*); while the broad peak B derives from the $j_{eff} = 3/2$ to the $j_{eff} = 1/2$ *UHB* transitions (as can be seen in Figure 1.4(d)). Finally, in Figure 1.5(c), the spectral weights of features in polarization dependent x-ray absorption spectra (XAS) are consistent

with an even superposition of the $|xy\rangle$, $|xz\rangle$, $|yz\rangle$ orbitals in the ground state.

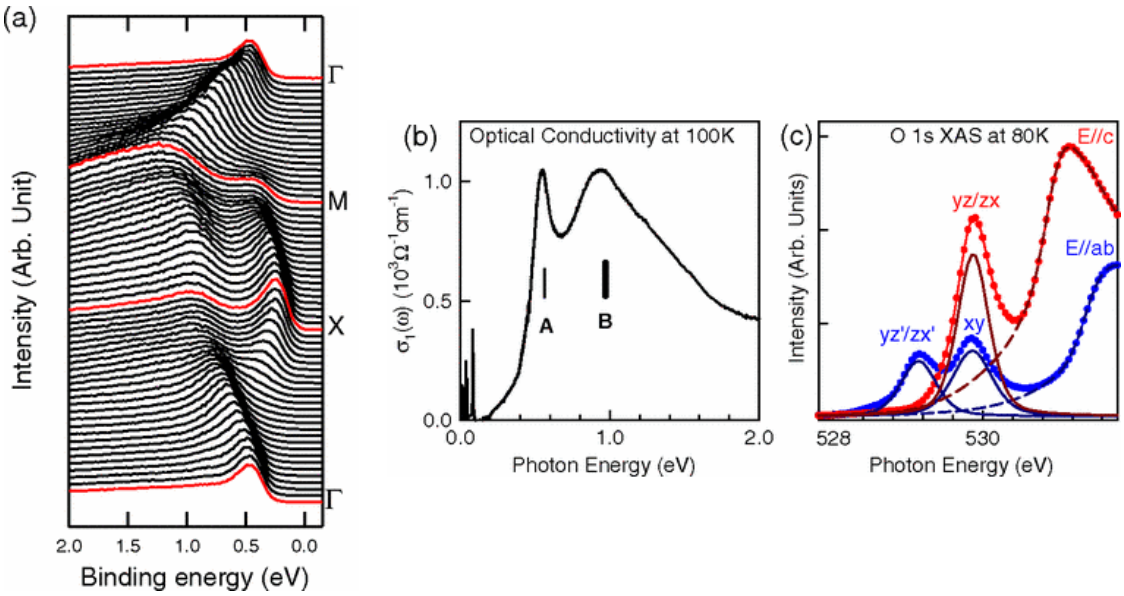

Figure 1.5: Experimental proof of the existence of the $j_{eff} = 1/2$ Mott insulating state in Sr_2IrO_4. (a) ARPES measurements show that bands disperse below Fermi level, (b) optical conductivity shows the presence of a finite gap and two peaks, A and B, corresponding to transitions from the occupied to the unoccupied bands, (c) Oxygen K-edge polarization dependent XAS spectra (dotted lines), compared with expected spectra (solid lines) under an assumption of equal-weighted orbitals. [Figures taken from Kim et al.[5]].

1.3 $CaIrO_3$

Among all iridate compounds, this work is focused on magnetic dynamics of $CaIrO_3$, an example of spin-orbit Mott insulator. In this section I will analyze some important physical aspects of this material.

1.3.1 Crystal and magnetic structure

$CaIrO_3$ single crystals are grown with the flux method of the group of Dr. Ohgushi in the Insitute for Solid State Physics of the University of Tokyo[9]. $CaIrO_3$ belongs to the orthorhombic space group $Cmcm(63)$ with lattice constants $a = 3.147$Å, $b = 9.863$Å and $c = 7.299$Å[25,26]. The crystal structure, a post-perovskite one, is reported in Figure 1.6(a). It is formed by IrO_6 octahedra connected to each other by sharing edge and corners along a and c axes, respectively, as shown in Figure 1.6(b,c), and are separated by Ca layers along b direction. The octahedra are compressed along the local z axis with a bond-length ratio of 0.97 and are alternatively rotated by 23° around the a axis[8].

Along the edge-sharing direction, pseudospins are ferromagnetically (FM) aligned, while along the corner-sharing direction they are antiferromagnetically (AFM) aligned, thus making $CaIrO_3$ an antiferromagnet with a Néel temperature of

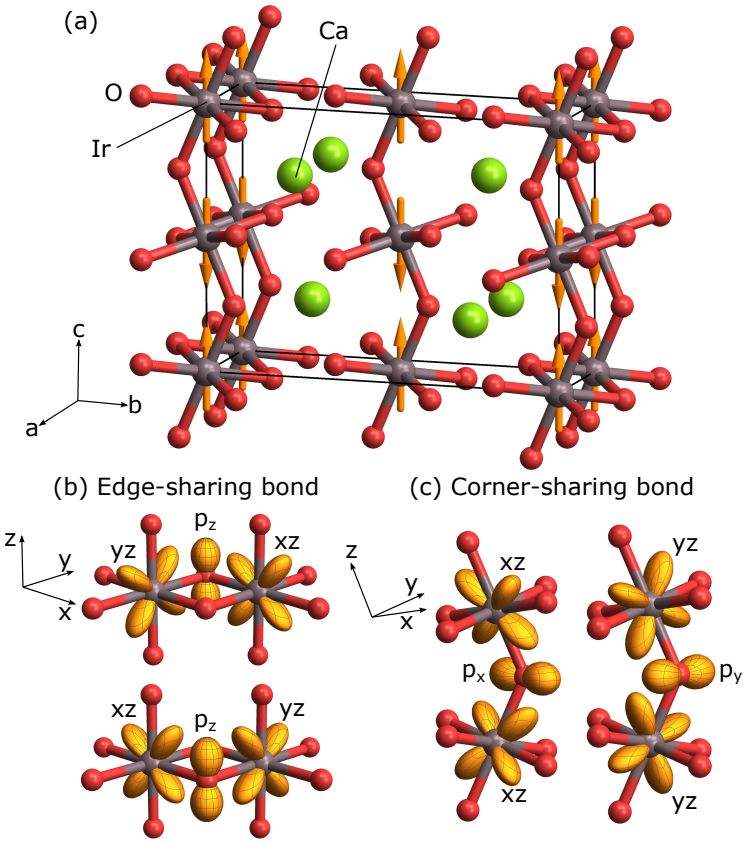

Figure 1.6: (a) Crystal structure of $CaIrO_3$: the iridium ions (gray spheres) are packaged in IrO_6 octahedra with oxygen ions (red spheres), that are separated by Ca layers along the b axis. The pseudospins (orange arrows) are ferromagnetically aligned along the a axis and antiferromagnetically aligned along the c axis. (b) Edge sharing bond-geometry along the a axis, with ferromagnetic alignment of pseudospins and C_{2h} point group symmetry. (c) Corner-sharing bond-geometry along the c axis, with antiferromagnetic alignment of pseudospins and C_{2v} point group symmetry. [Courtesy of M. Rossi].

$T_N \sim 110K$[8,27]. In addiction, magnetic moments are slightly canted along the b axis by an angle of $\sim 2°$[9,10], as can be understood from the parasitic ferromagnetism along this direction[9].

1.3.2 Bond-geometry dependent magnetic interactions

Iridates with $j_{eff} = 1/2$ Mott insulating state show a strong bond-geometry magnetic interactions. This is due to the fact that the $j_{eff} = 1/2$ ground state includes multiple orbitals with different hopping amplitudes to the neighboring ions.

Let us first consider corner-sharing geometry, where there is only one oxygen in common with two IrO_6 octahedra and the Ir-O-Ir angle is close to 180°. In this configuration only two t_{2g} orbitals participate to the bond, e.g. $|xy\rangle$ and $|xz\rangle$ orbitals along a bond in x direction[23] (look at Figure 1.7 (a)). It is predicted that, in the limit of strong SOC, the dominant magnetic contribution to exchange

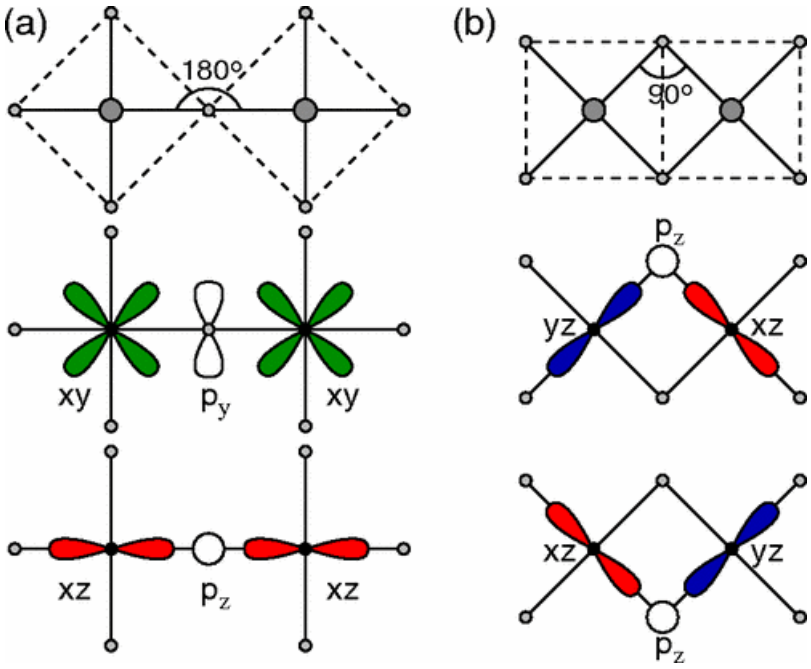

Figure 1.7: Corner-sharing (a) and edge-sharing (b) geometries of an IrO_6 octahedron. Different colors represent different t_{2g} orbitals, while large (small) dots stand for the transition metal (oxygen) ions. [Figure taken from Jackeli and Khaliullin[23]].

Hamiltonian is an isotropic Heisenberg term, as[23]

$$\mathcal{H}_{ij} = J\mathbf{S_i} \cdot \mathbf{S_j}, \tag{1.5}$$

where the spin moments are replaced by pseudospins with $j_{eff} = 1/2$ magnetic moment and J is the exchange constant. This Hamiltonian is well suited to describe magnetic interactions in iridium oxides with layered-perovskite structures, where iridium ions are arranged in 2D square lattices and the magnetic moments are AFM aligned, like Sr_2IrO_4[14,28,29], $Sr_3Ir_2O_7$[15,30,31] and Ba_2IrO_4[32,33].

In edge-sharing geometry, there are two oxygen in common with two IrO_6 octahedra and the Ir-O-Ir angle is close to 90°. Again, only two orbitals are active on a given bond, e.g. $|xz\rangle$ and $|yz\rangle$ orbitals along bonds in the xy plane[23] (look at Figure 1.7 (b)). In this case, however there are two possible paths for a charge transfer process, i.e. via lower or upper oxygen ion, whose amplitudes disruptively interfere such that the isotropic Heisenberg term exactly vanishes[23]. So, an otherwise negligible anisotropic part appears, depending on the spatial orientation of the bond. It can be demonstrated that for a given bond lying in the plane perpendicular to $\gamma = (x, y, z)$, the corresponding Hamiltonian is[23]:

$$\mathcal{H}_{ij}^{(\gamma)} = -JS_i^\gamma S_j^\gamma, \tag{1.6}$$

where $S_{i,j}^\gamma$ are the γ-components of the $s = 1/2$ operator for the pseudospins at lattice site i, j and J is the exchange constant. This Hamiltonian is the quantum analog of the *compass model*[34], that is the building block of the Kitaev model. The latter theory deals with $s = 1/2$ systems in honeycomb lattices, which interactions between nearest neighbors are Ising-like (XX, YY, ZZ link)[35]. Kitaev-like behavior

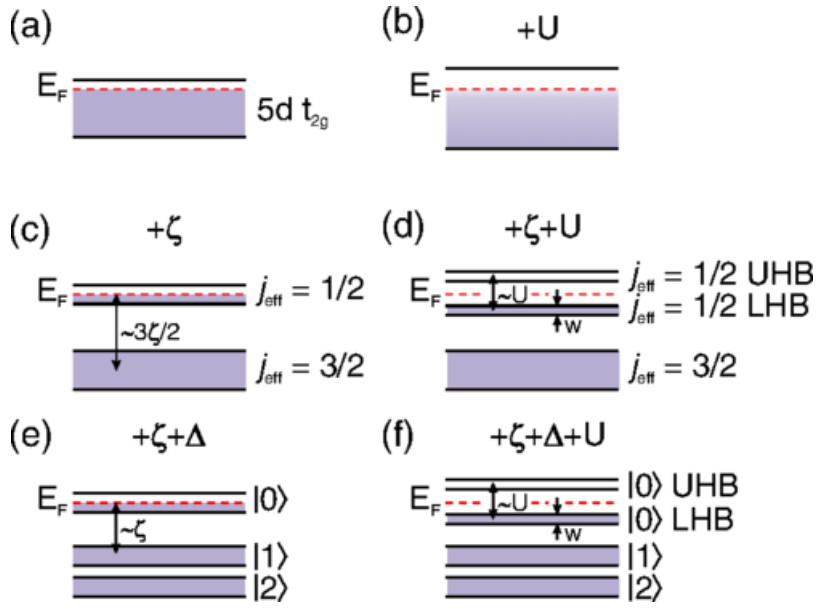

Figure 1.8: Schematic energy diagram of the outermost t_{2g} orbital in iridates with d^5 configuration (a), with Coulomb repulsion (b), with SOC (c), with both SOC and Coulomb repulsion (d), with SOC and tetragonal crystal field (e) and with all effects (SOC, tetragonal crystal field, Coulomb repulsion) taken into account (f). [Figure taken from Moretti Sala et al.[10]].

could be observed in A_2BO_3 compounds (where A and B are alkali and TM ions, respectively)[23], like Li_2RuO_3[36] and Na_2IrO_3[7].

$CaIrO_3$ features both corner- and edge-sharing bond geometries, but it remain to be understood if its magnetic interactions agree or not with previous models.

1.3.3 Beyond the $j_{eff} = 1/2$ ground state

From Equation 1.3, we can see that there is a competition between SOC and structural distortions of octahedral geometry, parameterized by constants λ and Δ, respectively. The theory developed by Jackeli and Khaliullin[23] is based on the following assumption

$$|\Delta| \ll \lambda \ll (10\ Dq)\,, \tag{1.7}$$

In $CaIrO_3$, tetragonal distortions are more pronounced compared to other iridates[37]. So the robustness of $j_{eff} = 1/2$ Mott insulating state could be undermined by the presence of this large distortion.

From RIXS (Resonant Inelastic X-ray Scattering) data taken at the L_3 edge of iridium ion, Moretti Sala et al.[10] have evaluated the value of the SOC constant and of the tetragonal crystal field, $\lambda = 0.52$ eV and $\Delta = -0.71$ eV, respectively. Since they are comparable in modulus, the basic assumption of the $j_{eff} = 1/2$ model is no longer valid, so it would now be useful to analyze the effect of the departure of the ground state of $CaIrO_3$ from the pure $j_{eff} = 1/2$ state.

Figure 1.8 shows the effect of adding electronic correlation (U) on the t_{2g} in the absence of SOC (a), with SOC (c) and also with the tetragonal distortion of the crystal field (e). In particular Figure 1.8(e) is relevant to the case of $CaIrO_3$ and

shows that the narrowing of the bands introduced by SOC is preserved. Also in this case, the introduction of a moderate U may drive the system into an insulating state. The effect of a large tetragonal crystal field is the splitting of the $j_{eff} = 3/2$ band, but has no impact on the width of the ground state. However the mixture of $|xy\rangle$, $|yz\rangle$, $|xz\rangle$ orbitals into the $CaIrO_3$ ground state is strongly uneven with possible consequences on the magnetic interactions.

Chapter 2

Resonant Inelastic X-ray Scattering

Resonant inelastic x-ray scattering (RIXS) is a *photon-in photon-out* spectroscopy and a powerful technique to investigate strong correlated electron systems.

In this Chapter, I will briefly review the general aspects of this spectroscopic technique, focusing on its use in $5d$ correlated electron compounds. More detailed reviews of RIXS can be found in Schülke[39] and Ament et al.[40].

2.1 General aspects of RIXS

RIXS is a technique that probes different types of excitations: in particular magnons and phonons in the meV range, plasmons, crystal-field and charge-transfer excitations in the eV range. Figure 2.1 sketches the characteristic excitations and the corresponding energy scales.

In this thesis, I will mostly focus on magnetic and crystal field excitations, which are the most informative on the nature of the magnetic and electronic correlations in strongly correlated electron systems. Magnetic excitations result from a perturbation of electron magnetic moment in the ordered magnetic lattice. Collective magnetic modes are called magnons and disperse throughout the whole Brillouin zone. The spectroscopic technique usually used to study magnetic properties of such materials

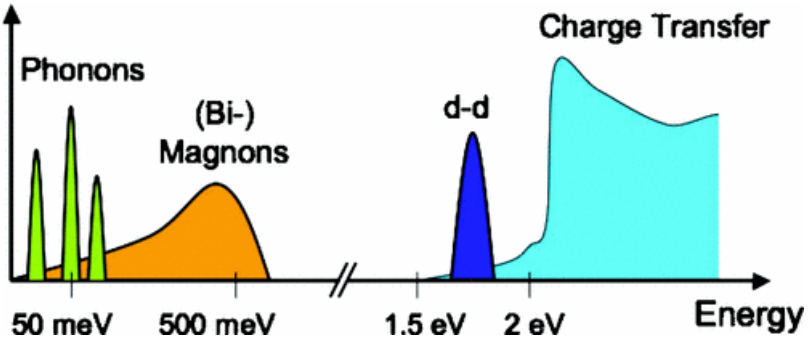

Figure 2.1: Energy scales of different elementary excitations in strongly correlated electron materials such as TMOs. [Figure taken from Ament et al.[40]]

is inelastic neutron scattering (INS)[41,42]. This technique has an energy resolution of fractions of meV and its scattering cross-section has a clear connection to the sample dynamical structure factor, which describes the magnetic dynamics in the system. Unfortunately, inelastic neutron scattering requires large-volume samples (several mm^3) and it cannot be used when the compound contains a strong neutron-absorbing material, such as iridium. In these cases, RIXS provides an alternative route[6]. Crystal field excitations, instead, are due to transitions between crystal field split states. In the case of TMOs, the active states are the transition metal *nd* orbitals and the corresponding transitions are often called *dd* excitations. Particularly interesting is the case of quasi-degenerate orbitals that give rise to orbital ordering. Collective orbital excitations (orbitons) can emerge and disperse over the whole Brillouin zone. It has been shown that RIXS can be used to probe orbitons[43,44].

Some of the important RIXS features are listed below:

- **Element and orbital specific:** element sensitivity can be achieved by tuning incident photons to a specific absorption edge of the material we want to study. RIXS is also able to distinguish between different chemical environments, in which ions have different valencies or occupy non-equivalent crystallographic positions, provided that there is a measurable shift in the absorption edge, i.e. larger than the experimental resolution. Figure 2.2 summarizes the main absorption edges of elements as a function of their atomic number.

- **Bulk sensitivity:** the penetration depth of x-rays depends on both material and scattering geometry, but is typically of the order of ≈ 50 μm for hard x-ray photons with energy ≈ 10 keV and ≈ 0.1 μm in the soft x-ray range. Thus we can, in first approximation, assume that RIXS mostly probe the bulk of the material. Some degrees of surface sensitivity can be obtained by selecting a suitable scattering geometry or by studying thin films or superlattices.

- **Small sample volumes:** photon-matter interaction is much stronger than that of neutron. In this respect RIXS is more convenient than inelastic neutron scattering because it does not require very large-volume samples. In many cases, the lateral dimension of the sample is limited by the x-ray spot size which typically amounts to ≈ 100 μm^2.

- **Charge neutrality:** RIXS is a photon-in photon-out technique and no charge is added to or removed from the sample, preserving charge neutrality of the system. This is very important when we study insulating samples, since charging issues are avoided.

- **Momentum resolution:** RIXS involves scattering of x-rays, with sizable momentum which can be transferred to the system during the scattering process. The momentum transfer $\hbar|\mathbf{q}|$ is equal to

$$\hbar|\mathbf{q}| \simeq \frac{4\pi\hbar}{\lambda}\sin(\theta), \tag{2.1}$$

where 2θ is the scattering angle, $\lambda_i \simeq \lambda_o \simeq \lambda$ is the wavelength of the incident and scattered x-rays. In hard x-rays, λ is comparable with the lattice

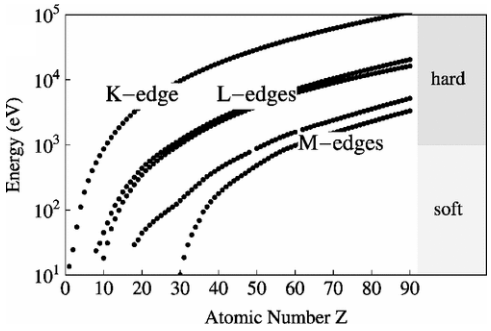

Figure 2.2: Energy of *K, L, M* x-ray absorption edges and their dependence on atomic number *Z*. X-rays below 1 keV are called soft x-rays, above hard x-rays[40].

parameters of solids, ≈ 1 Å, thus allowing to probe excitations over a sizable fraction of the Brillouin zone of the sample.

- **Polarization analysis:** the symmetry of excitations can be further inferred by looking at the polarization dependence of the RIXS cross section. Unfortunately, only few RIXS beamlines allow polarization analysis, at the expense of throughput and energy resolution, but there are many efforts in trying to overcome these difficulties.

There are two main limitations of the RIXS technique: it is photon hungry and its energy resolution is far from the standard of inelastic neutron scattering. The former limitation can be mitigated by performing experiments at third generation synchrotrons which are extremely brilliant source of x-rays. Concerning the energy resolution it should be noted that it has improved dramatically over the last decades and we expect it to improve further in the years to come. Nowadays RIXS experiments are routinely performed with energy resolution around 20 meV.

2.2 The RIXS process

During the scattering process, the incoming photon is scattered from a state with wave vector $\mathbf{k}$ and polarization ϵ into a state with wave vector $\mathbf{k}'$ and polarization ϵ'. A typical scattering geometry is presented in Figure 2.3. The two x-rays belong to the scattering plane. The polarization of the incoming (outgoing) photon can be decomposed into components parallel ϵ^{π} ($\epsilon^{\pi'}$) and perpendicular ϵ^{σ} ($\epsilon^{\sigma'}$) to the scattering plane. The angle between $\mathbf{k}$ and $\mathbf{k}'$ is the scattering angle, 2θ.

The microscopic picture of the RIXS process is shown in Figure 2.4. The scattering can be seen as a two-step process: starting from the ground state, the absorption of an x-ray photon promotes a core electron into an empty valence level. Since the energy of the incoming photon is very high (~ 10 keV), the system is left in an highly unstable state with a core hole. The lifetime of the intermediate state is typically of the order of $1-2$ fs. In RIXS one looks at the radiative decay of the core hole. From energy and momentum conservation follows that

$$\begin{aligned} \hbar\omega &= \hbar\omega' + E^{exc}, \\ \hbar\mathbf{k} &= \hbar\mathbf{k}' + \hbar\mathbf{q}, \end{aligned} \tag{2.2}$$

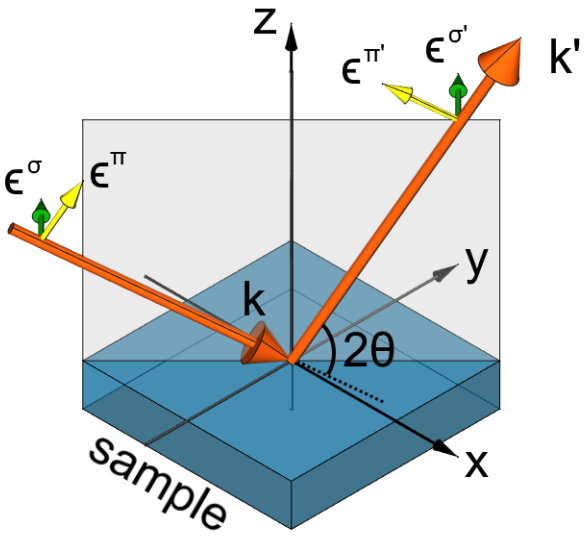

Figure 2.3: Typical scattering geometry in RIXS experiments. The incoming (outgoing) photons are described using their wave vectors $\mathbf{k}$ ($\mathbf{k}'$) (orange arrows) and polarization ϵ (ϵ'). The polarization can be decomposed into components parallel to scattering plane, ϵ^{π}, and perpendicular to it, ϵ^{σ}. The sample is represented by light blue box.

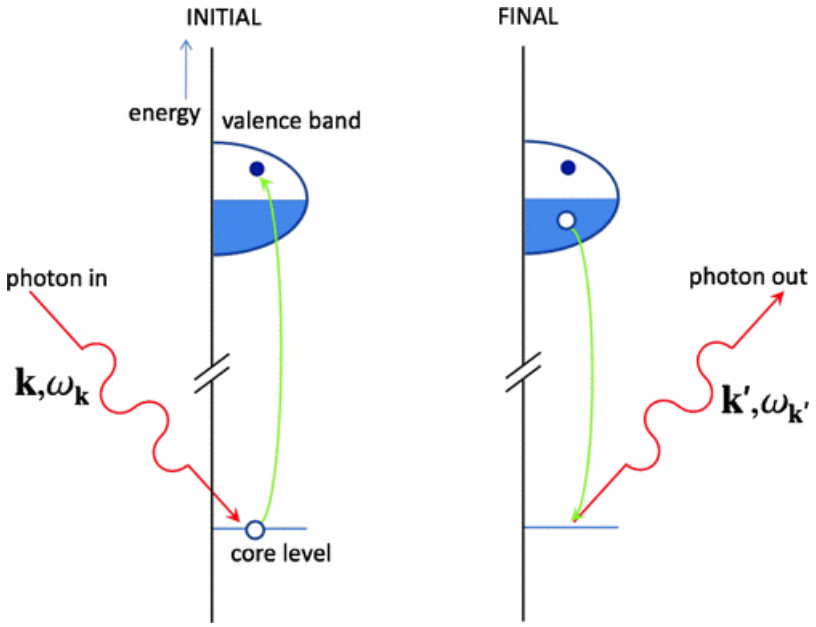

Figure 2.4: Schematic picture of the RIXS process. The incoming photon excites an electron from a core level to an empty valence band level. The empty core state is then filled by a valence electron under emission of a photon. The RIXS process creates a valence excitation with energy $\hbar\omega_{\mathbf{k}} - \hbar\omega_{\mathbf{k}'}$ and momentum $\hbar\mathbf{k}' - \hbar\mathbf{k}$. [Figure taken from Ament et al.[40]].

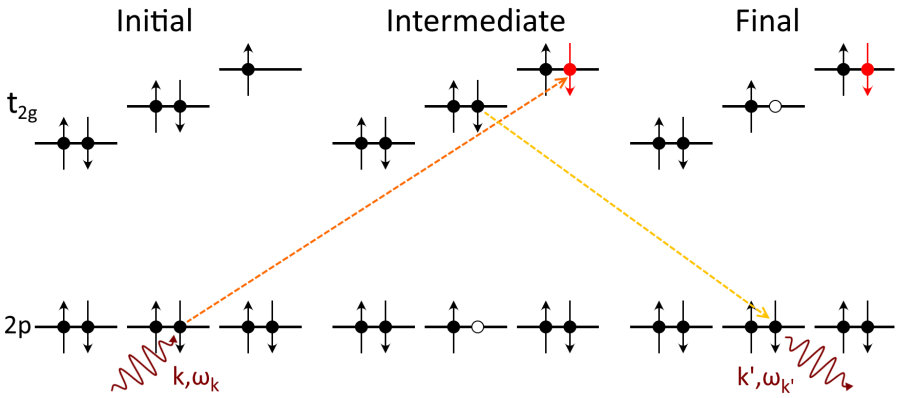

Figure 2.5: Spin-flip transition during a RIXS process in the case of L_3-edge of an iridate. The excited electron is depicted as a red arrow.

where $\hbar\omega$ ($\hbar\omega'$) and $\hbar\mathbf{k}$ ($\hbar\mathbf{k}'$) are energy and momentum of the incoming (outgoing) photon, respectively, E^{exc} is the energy transferred to the excitation.

An additional conservation law concern the angular momentum of the whole system and sets constraints on the photons polarization. If an excitation carries a finite momentum, the polarization of the scattered photons should be rotated with respect to the incident one. This is, for example, the case of magnetic excitations. The ability of RIXS of measuring magnetic excitations was not recognized in the early stages of this technique, but eventually brought RIXS to its current success[45,46]. The fact that spin-flip processes are allowed relies in the fact that the intermediate state is strongly spin-orbit coupled and therefore the spin magnetic moment does not need to be conserved (see Figure 2.5).

2.3 The RIXS cross section and the dynamical structure factor

In this section, I will try to link the RIXS scattering amplitude and the dynamical structure factor. To do that, I will first describe the formalism behind the RIXS cross section calculation and the physical meaning of its components. A complete and detailed derivation of the equation can be found in the reviews of Schülke[39] and Ament et al.[40].

The RIXS cross section can be expressed using the Kramers-Heisenberg generalized formula. In the dipole approximation, it leads to

$$\frac{d\sigma^2}{d\Omega\, d\hbar\omega_{\mathbf{k}'}} \approx \frac{\pi e^4}{2\epsilon_0^2 c^4}\omega_{\mathbf{k}}\omega_{\mathbf{k}'}^3 \sum_f \left| \sum_n \frac{\langle f|\, \mathcal{D}^\dagger\, |n\rangle \langle n|\, \mathcal{D}\, |g\rangle}{E_g + \hbar\omega_{\mathbf{k}} - E_n + i\Gamma_n} \right|^2 \times \delta\left(E_f - E_g + \hbar(\omega_{\mathbf{k}'} - \omega_{\mathbf{k}})\right), \tag{2.3}$$

where $|g\rangle = |g, \mathbf{k}, \epsilon\rangle$ is the ground state of the entire system, composed by the sample and the photon field, with energy $E_g = E_g + \hbar\omega_{\mathbf{k}}$. $|n\rangle$ is the intermediate state with energy E_n and lifetime broadening Γ_n. $|f\rangle = |f, \mathbf{k}', \epsilon'\rangle$ is the final state with energy $E_f = E_f + \hbar\omega_{\mathbf{k}'}$. $\mathcal{D}$ ($\mathcal{D}^\dagger$) is the dipole operator related to the absorption (emission) of a photon.

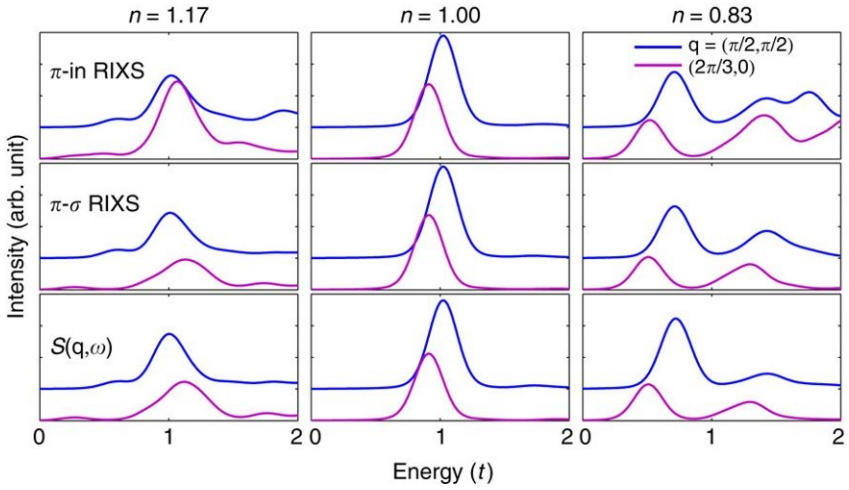

Figure 2.6: The RIXS cross section in different points in the reciprocal space at the Cu L_3 edge (top and middle panels) compared to the spin dynamic structure factor $S(\mathbf{q},\omega)$ (bottom panels). In particular, top panels show calculated RIXS cross sections for an incoming photon with polarization π and whatever outgoing polarization. Middle panels selects only cross-polarized channel to stress the magnetic nature of the excitations. [Figure taken from Jia et al.[47].]

From Equation 2.3, we see that the resonance condition

$$\hbar\omega_{\mathbf{k}} \simeq E_n - E_g \tag{2.4}$$

amplifies the RIXS cross section. The two-step nature of the RIXS process is related to the term at the numerator: first the electron is excited from the ground to the intermediate state, through the absorption of a photon ($\langle n|\,\mathcal{D}\,|g\rangle$), and then the de-excitation to the final state occurs through the emission of another photon ($\langle f|\,\mathcal{D}^\dagger\,|n\rangle$). The presence of the intermediate state is of fundamental importance in RIXS, since it allows transitions of electrons belonging to the same shell (e.g. *dd* excitations), even if they are dipole forbidden. Last thing to be noticed, the Dirac delta function imposes the conservation of energy during the whole process: the energy lost by the photon is entirely transferred to the excitation in the sample, $E^{exc} = E_f - E_g = \hbar(\omega_{\mathbf{k}'} - \omega_{\mathbf{k}})$.

Interestingly, in the specific case of Mott insulator with gapped charge excitations, the RIXS cross section can be approximated by the dynamical structure factor $S(\mathbf{q},\omega)$[47] which can be expressed as the imaginary part $\chi''(\mathbf{q},\omega)$ of a generalized susceptibility[48]

$$\frac{d\sigma^2}{d\Omega\, d\hbar\omega_{\mathbf{k}'}} \propto S(\mathbf{q},\omega) = -\frac{1}{\pi}\frac{1}{1-e^{-\omega/k_BT}}\chi''(\mathbf{q},\omega) \tag{2.5}$$

This approach is still very much debated, but in the case of cuprates it was widely used to compare calculations and experiments[47,49]. In Figure 2.6 Jia et al.[47] compare the calculated RIXS cross section and the spin dynamical structure factor in the case of Cu L_3-edge.

2.4 Experimental setup for resonant inelastic hard x-ray scattering

RIXS experiments take place at third generation synchrotron facilities. Synchrotron beamlines transport, focus and monochromatize the x-rays produced by the source, while a spectrometer is used to analyze photons scattered by the sample. In the following, I will provide the main figures of ID20, the hard x-ray RIXS beamline at the European Synchrotron Radiation Facility (ESRF,Grenoble,France), where I carried out my master thesis experiments.

The working principle of a synchrotron and the main figures of ESRF are the following: electrons are accelerated in a linear accelerator by an high-voltage alternating electric field to an energy of 200 MeV. The electrons then pass into the Booster synchrotron which is a radio-frequency cavity with a ring shape that accelerates electrons to 6.04 GeV. Once electrons have reached the target energy they are injected in the storage ring, where the circular trajectory is maintained by the action of several magnets that accelerate electrons, producing radiation.

The actual source of ID20 is a device called undulator, a periodic array of dipole magnets with an alternating magnetic field in the direction perpendicular to electron motion. Undulators emit linearly polarized radiation with a characteristic wavelength λ given by[50]

$$\lambda(\theta) \approx \frac{\lambda_u}{2\gamma^2}\left(1 + \frac{K^2}{2} + \gamma^2\theta^2\right), \tag{2.6}$$

where $\lambda_u = 26$ mm is the periodicity of the undulators, $\gamma = E/(mc^2) \approx 11.8 \cdot 10^3$ is the relativistic Lorentz factor, $K = eB\lambda_u/(2\pi mc) \approx 0.61$ is a parameter related to undulators deflection and θ is the observation angle. The undulators of ID20 cover an energy range between 4 and 20 keV.

2.4.1 Beamline ID20 at ESRF and the hard x-ray high-energy resolution RIXS spectrometer

A beamline is a collection of consecutive optical elements that focus and monochromatize the x-rays in their path from the source to the sample position. The ID20 optical layout is shown in Figure 2.7. Focusing is mainly performed by three optical elements: cylindrical mirror (CM1), toroidal mirror (FM2) and Kirkpatrick-Baez system (KB). The cylindrical mirror takes the divergent x-ray beam produced by the ondulators and collimate it in the vertical direction. The toroidal mirror focuses the beam to ≈ 50 μm$\times$300 μm (vertical $\times$ horizontal) at an intermediate position along the beamline and finally the KB system re-focuses the beam on the sample to a spot of ≈ 10 μm$\times$20 μm size. In order to monochromatize the beam, in the case of hard x-rays, monochromators exploit Bragg's reflection to narrow the bandwidth of the beam[51,52]. When one wants to operate in the low-energy resolution high-flux mode, x-rays are monochromatized only by means of nitrogen-cooled Si(111) pre-monochromator (pre-mono), whose intrinsic energy resolution is $\Delta E/E = 1.1 \cdot 10^{-4}$. If instead, one is interested in high-energy resolution, a system of post-monochromators (post-mono) can be added. For specific

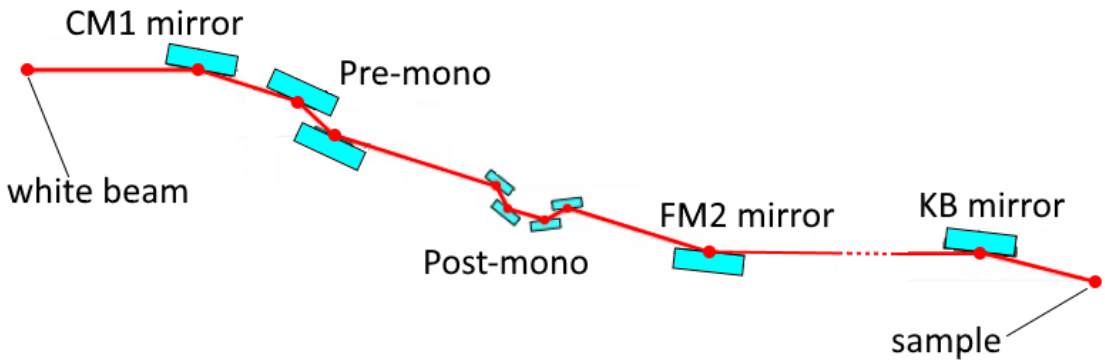

Figure 2.7: Optical layout of ID20 beamline at ESRF.

x-ray energies, backscattering channel-cut post-monochromators are available. In the case of Ir L_3-edge, ID20 is equipped with a Si(844) backscattering channel-cut post-monochromator with an intrinsic energy resolution $\Delta E/E = 1.6 \cdot 10^{-6}$. All the optical elements of the beamline are kept in ultra-high vacuum ($\approx 10^{-8}$ mbar) to maximize the photon flux on the sample. At Ir L_3-edge the photon flux amounts to $\approx 10^{12}$ photons/second in a bandwidth of ≈ 15 meV.

The focused monochromatic beam, whose polarization lies in the horizontal plane, is scattered by the sample and is collected by the spectrometer shown in Figure 2.8. The RIXS spectrometer is equipped with five Si(844) spherical diced crystal analyzers, that Bragg reflect the beam close to backscattering condition to select the scattered photon energy[53]. The choice of the analyzer depends on working energy, energy resolution and flux needed. Available Si(844) analyzers at ID20 have a diameter that ranges from 20 to 80 mm. The sample to analyzer distance can be varied from 1 to 2 m. During my experiments, I have used only one of the five analyzers, with 60 mm diameter, and sample to analyzer distance fixed to 1 m, collecting a solid angle of $\approx 2.8 \cdot 10^{-3}$ sr. The scattered beam is collected by a pixelate detector that is needed when we require both energy and momentum resolution in an experiment[54]. The sample (or the source of scattered radiation), the analyzer and the detector, lie on the same circumference, exploiting the so-called Rowland geometry, reported in Figure 2.9. Within this configuration, x-rays are reflected from the whole analyzer surface with the same Bragg angle and are all focused on the detector. So this geometry allows us to combine energy analysis and focusing in a single optical element. Finally, the analyzers and the detector are installed in a helium-filled chamber to reduce losses due to air scattering.

The spectrometer energy resolution is determined by different factors. The finite pixel size of the detector $p = 55$ μm gives a contribution to energy resolution of[54]

$$\frac{\Delta E_p}{E} = \frac{p}{2R \tan\theta_B} \approx 1.03 \cdot 10^{-6} \Rightarrow \Delta E_p \approx 24 \text{ meV}, \tag{2.7}$$

The contribution due to the finite source size is

$$\frac{\Delta E_a}{E} = \frac{s}{R \sin(\theta_B) \tan(\theta_B)} \approx 3.8 \cdot 10^{-7} \Rightarrow \Delta E_s \approx 8 \text{ meV}, \tag{2.8}$$

The incident photon bandwidth determined by the Si(844) backscattering channel-cut post-monochromator gives an energy resolution contribution of 15

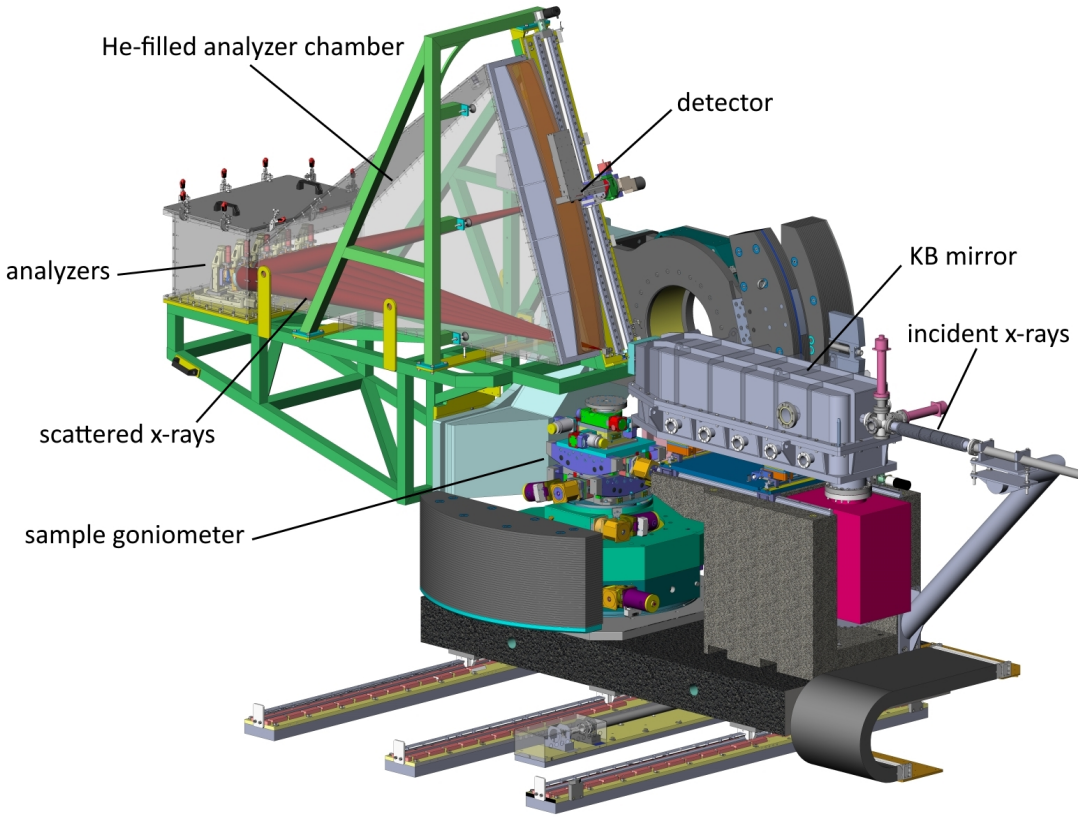

Figure 2.8: Sketch of ID20 RIXS spectrometer. [Courtesy of C. Henriquet].

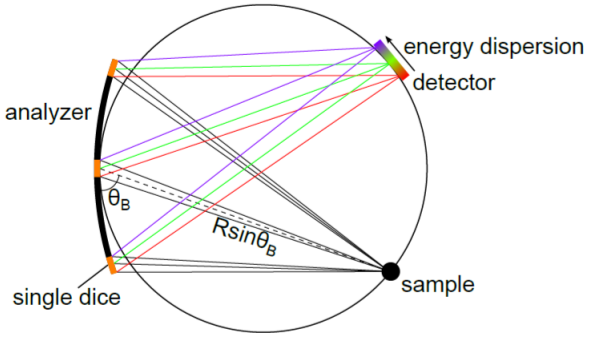

Figure 2.9: Rowland circle geometry used in ID20 RIXS spectrometer. The sample (or the radiation source), the analyzer and the detector lie on the same circumference of diameter R. The single cubes of diced crystal analyzer are colored in orange. In the figure are reported only three cubes for simplicity. Different energy scattered photons reach the detector at different positions due to dispersion properties of the analyzer. [Figure taken by Rossi[24]]

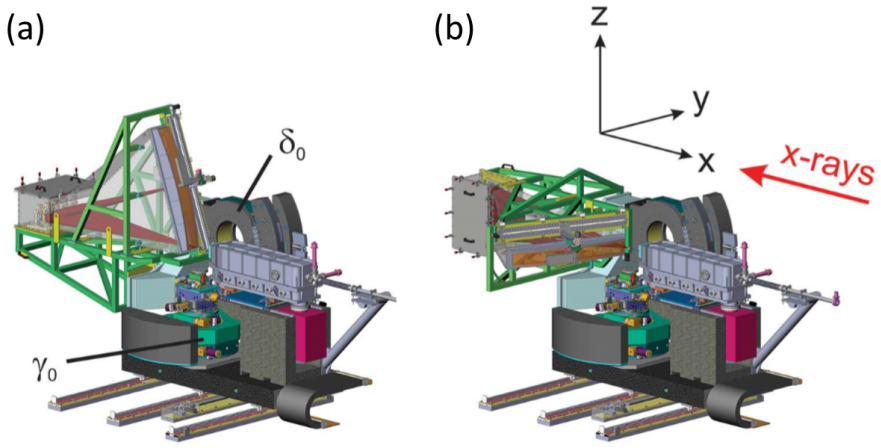

Figure 2.10: Possible scattering geometries of the RIXS spectrometer with $R = 2$ m for $\gamma_0 = 0$ and $\delta_0 = 0$ in both (a) and (b) panels. In (a) the RIXS spectrometer is in the position to scatter in the horizontal plane, while in (b) the spectrometer is rotated by 90° around the source-middle analyzer direction to scatter in the vertical plane. All combinations of these two geometries are possible. [Figure taken from Moretti Sala et al.[11]].

meV. Finally, the analyzer contribution is exactly the same of the previous one, since analyzers are Si(844) crystals. The overall energy resolution is ≈ 35 meV (at the Ir L_3-edge).

2.4.2 Momentum resolution

As said before, the dependence of RIXS spectra on momentum transfer is not negligible. The positions of the spectrometer fixes the scattered wave vector $\mathbf{k}_o$ and thus the scattering plane. The sample position defines the projection of the momentum transfer into the sample reciprocal space. For these reasons, in order to reach an arbitrary momentum transfer, the spectrometer has to rotate in both the horizontal and the vertical direction, as depicted in Figure 2.10, and the sample stage necessitate all the rotational degrees of freedom.

With the reference system defined in Figure 2.10, the momentum transfer in the laboratory frame is given by[11]

$$\mathbf{q}^{2\theta} = 2\pi \left(\frac{\hat{\mathbf{x}}}{\lambda_i} - \frac{\mathcal{T}^{2\theta}\hat{\mathbf{x}}}{\lambda_o} \right), \tag{2.9}$$

where $\mathcal{T}^{2\theta} = \mathcal{R}_{\hat{\mathbf{z}}}(\gamma)\mathcal{R}_{\hat{\mathbf{y}}}(\delta)$ is the transformation matrix describing the rotation of the 2θ-scattering arm by an angle γ around the z axis and by an angle δ around the y axis. Using the $\mathcal{UB}$ matrix formalism (see Appendix A), $\mathbf{q}^{2\theta}$ can be projected in the sample reciprocal space by the following matrix multiplication[11]

$$\mathbf{q}^{hkl} = (\mathcal{T}^{\omega\chi\varphi}\mathcal{UB})\,\mathbf{q}^{2\theta}, \tag{2.10}$$

where $\mathcal{T}^{\omega\chi\varphi} = \mathcal{R}_{\hat{\mathbf{z}}}(\omega)\mathcal{R}_{\hat{\mathbf{x}}}(\chi)\mathcal{R}_{\hat{\mathbf{y}}}(\varphi)$ describes the sample rotations, $\mathcal{B}$ defines a Cartesian frame in the sample reciprocal space and it depends on lattice parameters,

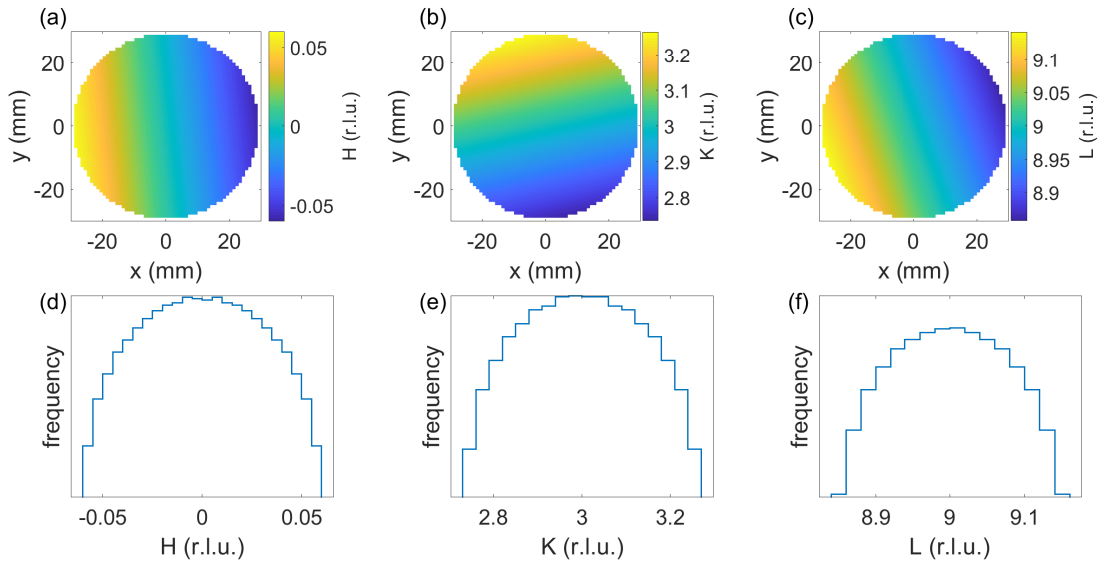

Figure 2.11: Momentum resolution distributions in the case of Ir L_3-edge of $CaIrO_3$ ($a = 3.147$Å, $b = 9.863$Å and $c = 7.299$Å). Sample and spectrometer are aligned to probe a momentum transfer of $\mathbf{Q} = (0, 3, 9)$ r.l.u. Panels (a),(c) and (e) show the momentum transfer spread along the reciprocal lattice directions over the analyzer surface with a diameter of $A = 60$ mm and $R = 1$ m. Panels (b),(d) and (f) show the widths of the momentum resolution functions.

and $\mathcal{U}$ connects laboratory and sample frames and it is determined during sample alignment.

The finite opening of the crystal analyzers introduces uncertainties on scattering arm angles, $\Delta\gamma$ and $\Delta\delta$, and so a finite momentum resolution. An estimate of the momentum resolution is given below in the case of quasi-elastic scattering[11]

$$\Delta\mathbf{q}^{hkl} \simeq \left(\mathcal{T}^{\omega\chi\varphi}\mathcal{U}\mathcal{B}\right)^{-1}\mathcal{T}^{2\theta}\Delta\mathbf{q}^{2\theta}, \tag{2.11}$$

where $\Delta\mathbf{q}^{2\theta} = 2\pi\left(0, -\Delta\gamma\cos(\delta_i), \Delta\delta\right)/\lambda$. As an example, let us take the case of $CaIrO_3$ single crystal at the momentum transfer $\mathbf{q}^{hkl} = (0, 3, 9)$ r.l.u.. Figures 2.11(a), (b) and (c) show the momentum transfer dispersion over the analyzer surface. The corresponding momentum transfer distributions are reported in Figures 2.11(d), (e) and (f) for the three directions in reciprocal space and show that the momentum resolution is small, but not negligible. Indeed, in this case, the variation along H amounts to ± 0.06 r.l.u., along K to ± 0.26 r.l.u. and along L to ± 0.14 r.l.u. I will show in the following that the momentum resolution should be taken into account for a correct interpretation of the experimental data.

Chapter 3

Magnetic dynamics of $CaIrO_3$ probed with RIXS

In this Chapter, I will focus on the magnetic dynamics of $CaIrO_3$ making use of RIXS spectra taken at Ir L_3-edge and collected at ID20 at ESRF. In the first part, I will look at the temperature dependence of the low-energy features of the RIXS spectra of $CaIrO_3$. After that, I will investigate their momentum dependence and I will propose a model to interpret the magnetic excitations in this material.

3.1 Principal features of RIXS spectra of $CaIrO_3$

A typical Ir L_3-edge RIXS spectrum of $CaIrO_3$ is shown in Figure 3.1 for energy losses up to 1.8 eV. Excitations above 0.35 eV have already been discussed by Moretti Sala et al.[10]. Features δ_1 and δ_2 are centered at ≈ 0.65 eV and ≈ 1.22 eV, respectively, and have been assigned to transitions between crystal field split states[10,55,56]. In particular, using the energy diagram and notation of Figure 1.8, the feature δ_1 can be ascribed to the transition from $|0,\pm\rangle$ ground state to $|1,\pm\rangle$ excited state, while the feature δ_2 to the transition from $|0,\pm\rangle$ to $|2,\pm\rangle$[10]. The nature of feature ξ, centered at ≈ 0.42 eV, is still debated. Gretarsson et al.[55] suggest that it comes from an excitation of an electron-hole pair across the charge gap; however the energy of the excitations does not match the size of the charge gap (≈ 0.34 eV)[8], thus casting out this interpretation. Another theory from Plotnikova et al.[57] grants the origin of the feature ξ to a combined effect of superexchange and Jahn-Teller interactions.

Here, I will only focus on the excitations below 0.35 eV. From Figure 3.1, we notice that their intensity profile is highly asymmetric and shows a continuous distribution. In the next sections, I will investigate both temperature and momentum dependence of such low-energy excitations.

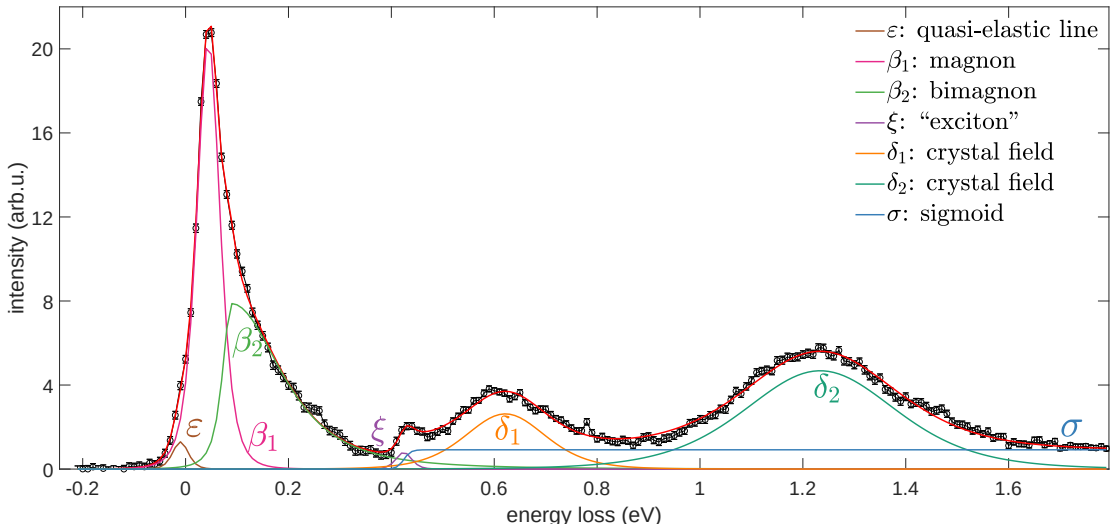

Figure 3.1: A generic RIXS spectrum of $CaIrO_3$ at the Ir L_3-edge measured at momentum transfer $\mathbf{Q} = (0, 3, 8)$ r.l.u. and at temperature $T = 40$ K (black line and circles). The red solid line reports the best-fit. The single function used in the fit (see Appendix B) are also reported.

3.2 Temperature evolution of magnetic excitations in $CaIrO_3$

To understand the nature of low-energy excitations below 0.35 eV, I analyze the evolution in temperature of their intensity. A collection of RIXS spectra of $CaIrO_3$ at momentum transfer $\mathbf{Q} = (1, 2, 9)$ r.l.u. is plotted in Figure 3.2 as a function of temperature, in a range from 20 K to 250 K. From the stack plot in panel (a), I notice that the RIXS intensity clearly shows a strong temperature dependence. In order to highlight this fact and to introduce the following data analysis, RIXS spectra are reported in a map in Figure 3.2(b). From the RIXS map, we extract two important observations:

i. the quasi-elastic (ε) line is peaked at the transition temperature, $T_N \approx 110$ K;

ii. the intensity of the feature centered at 45 meV energy loss, β_1, is suppressed above T_N.

As for what concern the ε peak, a detailed analysis is reported in Figure 3.2(c), which shows the normalized integrated intensity of the RIXS map in the energy region between -0.02 and 0.02 eV (black solid line). For comparison, I report also the AC dynamic magnetic susceptibility, χ''_m (red solid line), measured at 10 kHz by Gunasekera et al.[58]. Below the Néel temperature, the temperature dependence of ε resembles that of χ''_m. Above the transition temperature, instead, ε and χ''_m behaves differently: the dynamic magnetic susceptibility rapidly vanishes, while the ε peak has a much more pronounced tail. This comparison suggests that ε might have magnetic origin.

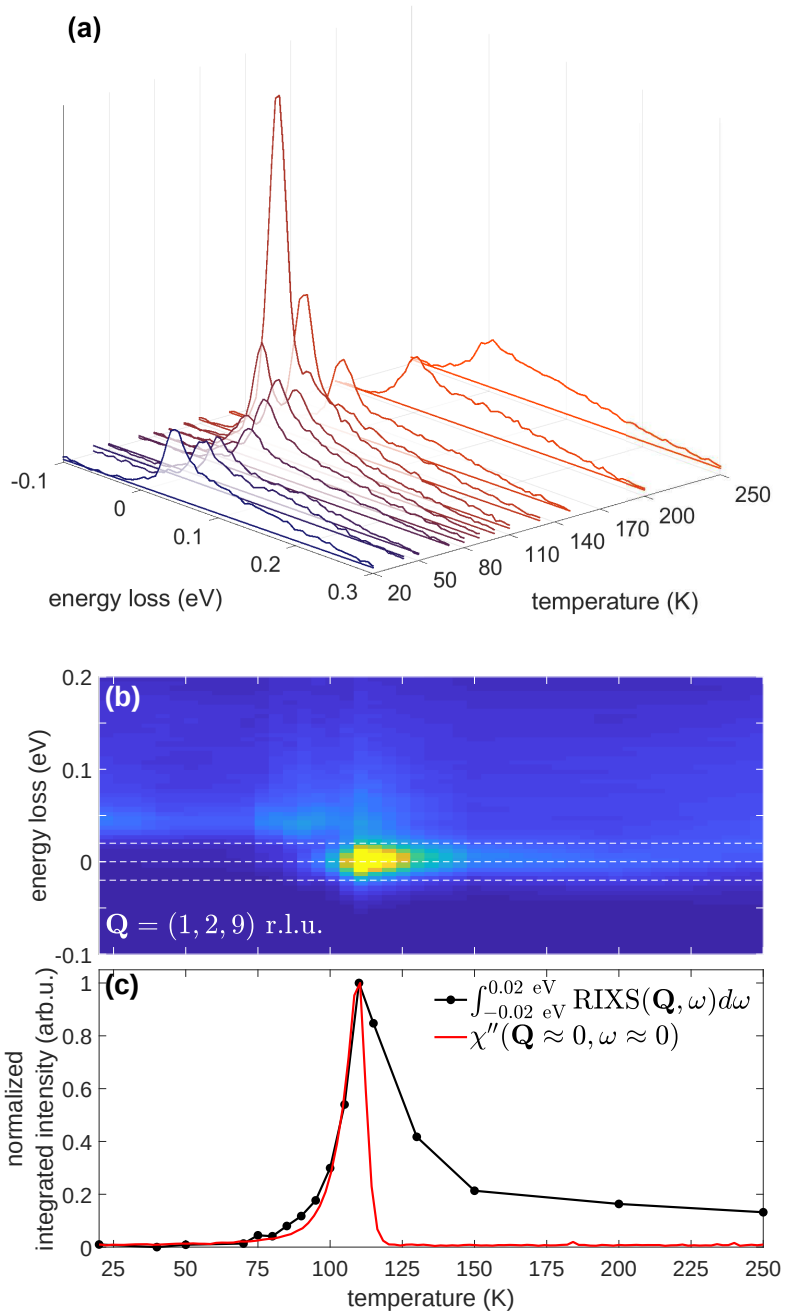

Figure 3.2: (a) Stack plot of the temperature dependence of RIXS spectra measured at momentum transfer $\mathbf{Q} = (1, 2, 9)$ r.l.u. (b) Map of the temperature evolution of RIXS spectra measured at momentum transfer $\mathbf{Q} = (1, 2, 9)$ r.l.u. The energy loss axis is limited in the region $(-0.1, 0.2)$ eV to highlight low-energy excitations. Top and bottom white dotted lines represent upper and lower limits of integration, whereas middle dotted line points out the 0 eV values. (c) Normalized integrated intensity of panel (a) from -0.02 eV to 0.02 eV (black line). It is also reported the imaginary part of AC dynamic susceptibility $\chi''(\mathbf{Q}, \omega)$ measured at a frequency of 10 kHz (red line) by Gunasekera et al.[58]. Both curves are normalized to unit area.

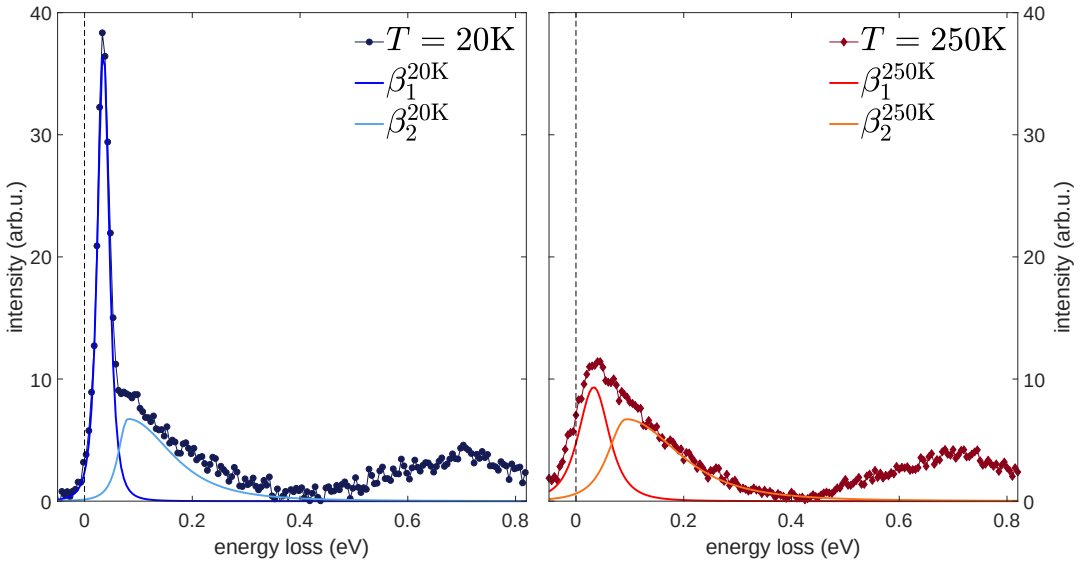

Figure 3.3: RIXS spectra reported are recorded at $T \ll T_N$ (dark blue line) and $T \gg T_N$ (dark red line). β_1 and β_2 curves are also reported for the two different temperatures (blue and light blue curves at $T = 20$ K, red and orange lines at $T = 250$ K, respectively). It is evident that β_2 has a less pronounced dependence on temperature with respect to β_1.

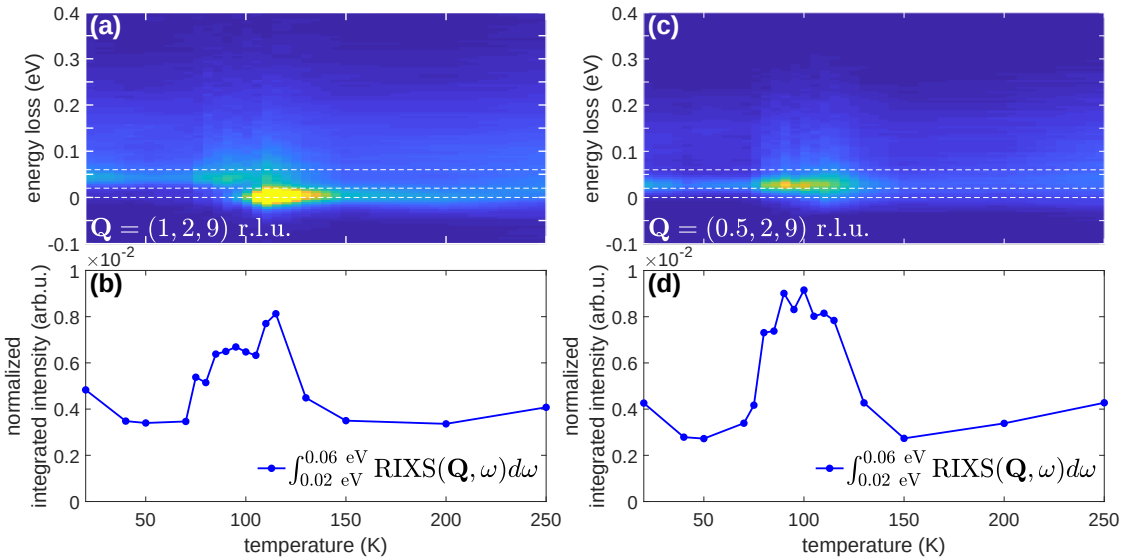

Figure 3.4: (a) Map of evolution in temperature of intensity of the low-energy excitations at momentum transfer $\mathbf{Q} = (1, 2, 9)$ r.l.u. Color scale is tuned to highlight the presence of β_1. Bottom and middle white dashed lines are the limits of integration. Bottom white line indicates 0 eV. (b) Normalized integrated intensity from 0.02 eV to 0.06 eV of panel (a). (c) Same as panel (a), but at momentum transfer $\mathbf{Q} = (0.5, 2, 9)$ r.l.u. (d) Normalized integrated intensity from 0.02 eV to 0.06 eV of panel (c). Curves of panels (b) and (d) are normalized to unit area.

The feature β_1 broadens with temperature and becomes unresolved above $T \gtrsim 95$ K because it overlaps in energy with features ε and β_2. From Figure 3.4(a) and (b), I note that features β_1 and β_2 overlap in energy. Instead, I observe that β_2

intensity (light blue and orange curves) is approximately constant in temperature. In Figure 3.4 I report the RIXS map and the integrated intensity of β_1 at both momentum transfer $\mathbf{Q} = (1, 2, 9)$ r.l.u. and $\mathbf{Q} = (0.5, 2, 9)$ r.l.u. The latter is very informative because ε is highly suppressed (see Figure 3.4(c)) thus making β_1 more visible. From Figure 3.4(d), it can be clearly seen that the temperature dependence of β_1 shows a broad peak slightly below the Néel temperature. Accordingly, also β_1 might have magnetic origin.

Before concluding on the magnetic nature of the low-energy excitations in $CaIrO_3$, in the next section I will investigate their momentum dependence along the principal crystallographic directions.

3.3 Momentum dependence of magnetic excitations of $CaIrO_3$

All the spectra treated in this section are collected at a temperature of 40 K, far below the Néel temperature of $CaIrO_3$. Referring to Figure 3.5, it can be observed that low-energy excitations present a characteristic dispersion relation along the three crystallographic directions in the sample reciprocal space. Along the edge-sharing H direction (Figure 3.5(a)), RIXS spectra display a modest momentum dependence. The maximum of the low-energy distribution is peaked at ≈ 25 meV at momentum transfer $\mathbf{Q} = (0.5, 2, 9)$ r.l.u. and disperses by about 17.4 ± 0.7 meV with a periodicity of 1 r.l.u. Along the K direction (Figure 3.5(c)), we do not observe any momentum dispersion. Finally along the corner-sharing L direction (Figure 3.5(d)), RIXS spectra show a peculiar momentum dependence: the low-energy boundary of the broad intensity distribution (the β_1 feature discussed above) is peaked at ≈ 44.4 meV at momentum transfer $\mathbf{Q} = (0, 3, 9)$ r.l.u. It has a dispersion of about 121.2 ± 3.0 meV with a periodicity of 1 r.l.u.. Instead the high-energy tail of the distribution has a momentum dependence with double periodicity in reciprocal space. Quantitative values for the dispersion of the β_1 feature were extracted by fitting the data using the method described in Appendix B. A summary of the fitting results is reported in panels (b), (d) and (f) of Figure 3.5.

I note that the momentum dependence of $CaIrO_3$ along the corner-sharing direction (Figure 3.5(e)) is very similar to the inelastic neutron scattering spectrum of $CuSO_4{\cdot}5D_2O$, shown in Figure 3.6. Mourigal et al.[59] assigned the origin of the excitation to the two- and four-spinon continuum. Based on the temperature dependence of RIXS spectra discussed above and in view of this analysis, I therefore conclude that the origin of the low-energy excitations in $CaIrO_3$ is magnetic, possibly has a pronounced two-spinon like character.

Spinons are quasi-particles carrying a spin quantum number of $s = 1/2$ each and are created from the fractionalization of magnons ($s = 1$)[61]. One can think about spinons as one-dimensional domain walls confined within the chain, freely to propagate along it[61,62]. If the spin chain is not perfectly Ising-like, the dispersion relation will exhibit some modulations. The two-spinon excitation forms a continuous distribution, arising from the sum of the dispersion relations of two single spinons, with characteristic momentum dependence and dynamic structure factor[59,60,63]. Two-spinon excitations have been detected in many inelastic neu-

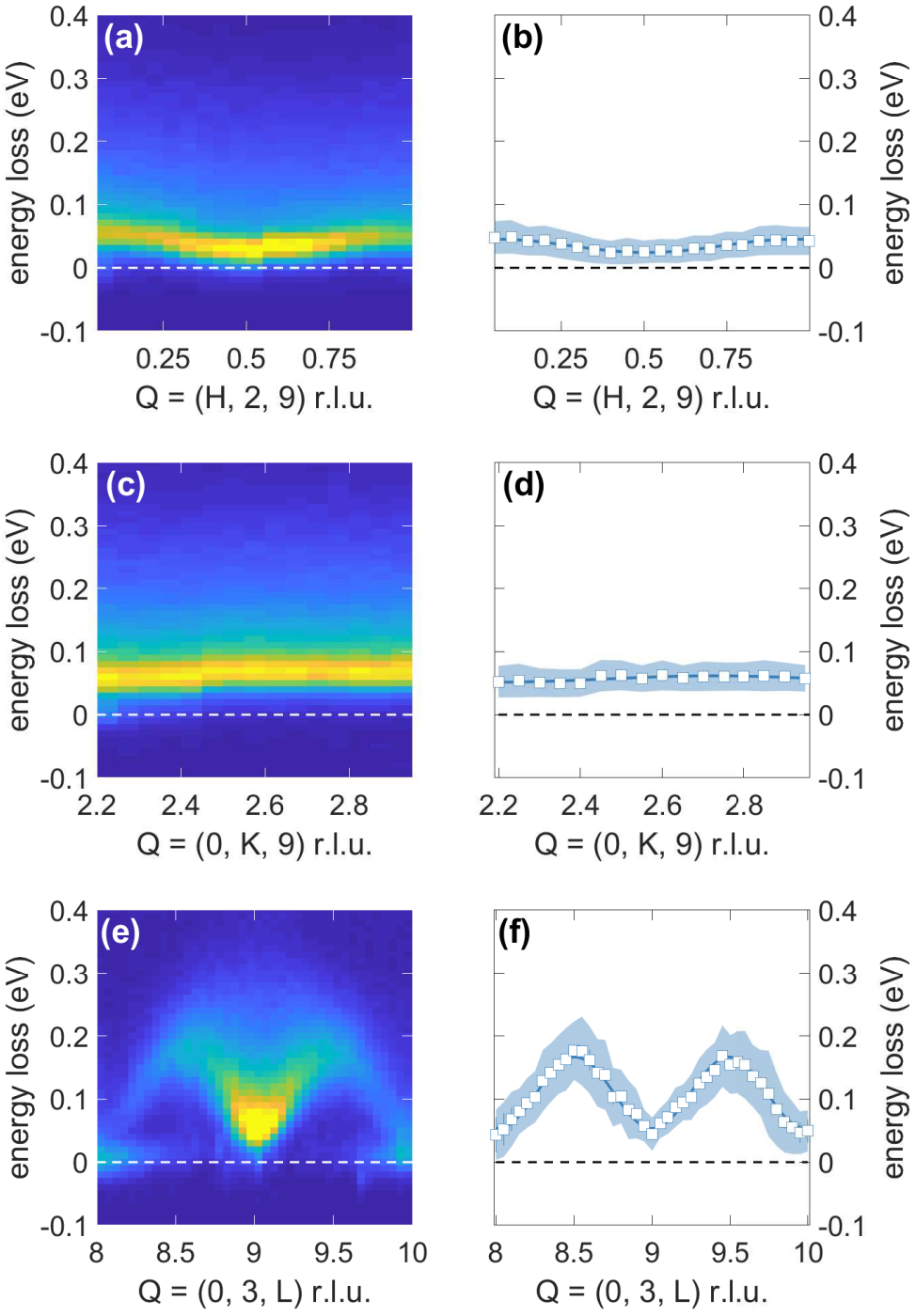

Figure 3.5: Momentum dependence of the low-energy excitations of $CaIrO_3$. Panels (a), (c) and (e) report RIXS raw data measured along H, K and L, respectively, corresponding to high symmetric directions of the sample reciprocal space. Panels (b), (d) and (f) represent the energy positions of the dispersion of β_1 (white squares). A simple sine function simulate the dispersion (blue solid line). The blue areas around the withe squares report the FWHM of β_1. All these spectra have been recorded at $T = 40$ K.

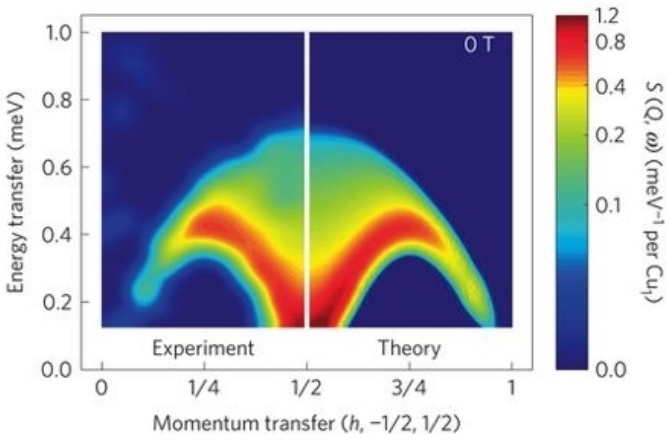

Figure 3.6: Inelastic neutron scattering spectrum of $CuSO_4 \cdot D_2O$ (right panel) and two- and four-spinon dynamic structure factor for the $s = 1/2$ Heisenberg antiferromagnetic chain (left panel). [Figure from Mourigal et al.[59]].

tron scattering experiments on numerous compounds (among which, for example, $KCuF_3$[64], $LiCuVO_4$[65] and the aforementioned $CuSO_4 \cdot 5D_2O$[59]).

In the two-spinon model, excitations live on a magnetic chain and do not interact with the magnetic moments on neighboring chains. Therefore, a simple two-spinon model cannot explain the experimental observation of a small, but finite momentum dependence of low-energy excitations along the H direction (see Figure 3.5(a) and (b)), which is indicative of some coupling between the magnetic chains. Moreover, resonant x-ray diffraction measurements by Ohgushi et al.[9] show that magnetic moments belonging to different chains couple ferromagnetically. In addiction, both a theoretical model by Jackeli and Khaliullin[23] and *ab initio* quantum chemical calculations by Bogdanov et al.[66] predict a weak ferromagnetic interaction along the edge-sharing direction, i.e. between the magnetic chains, in agreement with experiments. However, an experimental estimate of the magnetic couplings is missing and, despite the fact that $CaIrO_3$ is a long-range ordered magnet, it remains to be verified that the magnetism of $CaIrO_3$ is mostly one dimensional, i.e. largely dominated by a strong AFM interaction along the chain direction.

In the following, I will try to model the RIXS cross section in terms of the two-spinon dynamic structure factor in order to extract quantitative information about the magnetic couplings of $CaIrO_3$.

3.4 2D-extended two-spinon dynamic structure factor

The dynamic structure factor of a magnetic chain depends on the detail of the Hamiltonian describing the magnetic interactions. In the following, I base my analysis on the work of Müller et al.[67], and adopt the two-spinon dynamic structure factor for the Heisenberg chain, in which magnetic interactions are isotropic. Then, I will include the effect of a finite ferromagnetic coupling between the chains in the

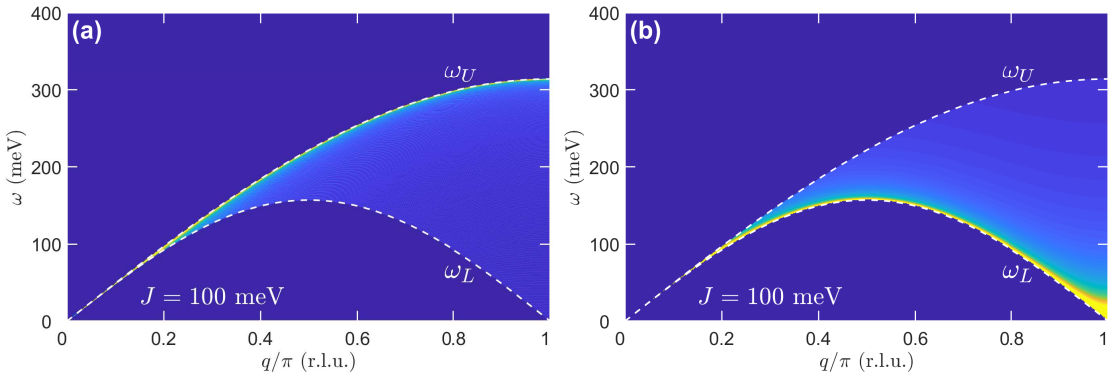

Figure 3.7: (a) Two-spinon density of states as calculated by Müller et al.[67] and reported in Equation 3.2. White dashed lines correspond to the lower and upper boundaries of the two-spinon continuum, ω_L and ω_U, as given by Equation 3.3. (b) Two-spinon dynamic structure factor $S_{uc}(\mathbf{q}, \omega)$ calculated from Equation 3.4

Random Phase Approximation[68].

The 1D $s = 1/2$ Heisenberg chain is described by the following Hamiltonian

$$\mathcal{H} = J_c \sum_{l=1}^{N} \mathbf{S}_l \cdot \mathbf{S}_{l+1}, \tag{3.1}$$

where J_c is the exchange coupling along the chain direction and $\mathbf{S}$ is the spin operator. A special class of eigenvalues of such Hamiltonian is characterized by[67]

$$\omega_m(q_z) = \pi J_c \sin\left(\frac{q_z}{2}\right) \cos\left(\frac{q_z}{2} - \frac{q_m}{2}\right), \tag{3.2}$$

where $0 \leq q_z \leq \pi$[1] is the projection of the momentum transfer along the spin chains direction and forms a continuum for $0 \leq q_m \leq q_z$. Its density of states is mapped in Figure 3.7 and it is bounded by the two curves[67]

$$\begin{aligned} \omega_L(q_z) &= \frac{\pi}{2} J_c \sin(q_z) \\ \omega_U(q_z) &= \pi J_c \sin\left(\frac{q_z}{2}\right) \end{aligned} \tag{3.3}$$

also reported in Figure 3.7(a) as white dashed lines. From the map, it is clearly seen that the two-spinon excitation is gapless in this model.

The corresponding (approximated) dynamic structure factor $S_{uc}(\mathbf{q}, \omega)$ is given by[67]

$$S_{uc}(\mathbf{q}, \omega) = \frac{\Theta(\omega - \omega_L(q_z))\Theta(\omega_U(q_z) - \omega)}{\sqrt{\omega^2 - \omega_L^2(q_z)}}. \tag{3.4}$$

and it is reported in Figure 3.7(b). I neglect the contribution of higher-order spinon excitations (four-spinons, etc.) based on the fact that, from theoretical calculations, the amount of spectral weight carried by higher order spinon amounts to 27 %.

[1] $\mathbf{q}$ is equal to the momentum transfer labeled by $\mathbf{Q}$, expressed in units of π ($\mathbf{q} = \pi\mathbf{Q}$).

Then, how could we take into account any possible coupling among the spin chains? Following the work of Bocquet et al.[68], I use the RPA model to calculate the dynamic magnetic susceptibility of coupled spin chains ($\chi_{cc}(\mathbf{q},\omega)$) from that of uncoupled spin chains ($\chi_{uc}(\mathbf{q},\omega)$). In the specific case of $CaIrO_3$, $\chi_{cc}(\mathbf{q},\omega)$ can be expressed as

$$\chi_{cc}(\mathbf{q},\omega) = \frac{\chi_{uc}(q_z,\omega)}{1 - 2J_a\cos(q_x)\chi_{uc}(q_z,\omega)} \tag{3.5}$$

where J_a and q_x represent the exchange coupling and the momentum transfer along the edge-sharing direction. Since the dynamic structure factor is related to the dynamic magnetic susceptibility by

$$S(\mathbf{q},\omega) = -\frac{1}{\pi}\frac{1}{1-e^{-\omega/k_BT}}\chi''(\mathbf{q},\omega), \tag{3.6}$$

where $\chi''(\mathbf{q},\omega)$ is the imaginary part of the dynamic magnetic susceptibility, we can calculate the dynamic structure factor for coupled chains $S_{cc}(\mathbf{q},\omega)$. The Bose-like factor takes into account the effect of finite temperature.

A similar model has already been applied in the study of magnetic interactions of inelastic neutron scattering spectra of $KTi(SO_4)_2$ by Nilsen et al.[69] and of Sr_3CuPtO_6 by Leiner et al.[70]. They used the spin dynamic structure factor of uncoupled spin chains ($S_{uc}(\mathbf{q},\omega)$) from Caux and Hagemans[63] and Equation 3.6 to simulate the spin dynamic structure factor of coupled spin chains ($S_{cc}(\mathbf{q},\omega)$), obtaining a satisfactory agreement between experiments and simulations.

3.5 The effect of the finite momentum resolution on spin dynamic structure factor

The two-spinon continuum described above is gapless[61,62], while experimental data feature a finite gap in the excitation spectrum of $CaIrO_3$. This effect cannot be accounted for by the coupling between spin chains, as it can be seen in the works of Bocquet et al.[68] and Leiner et al.[70]. I anticipate that the origin of the gap observed experimentally is likely due to the finite momentum resolution of the RIXS experiment which I analyze in the following.

In Figure 3.8(a), I report the distribution of the momentum transfer across the analyzer surface, when it is nominally centered at $\mathbf{Q} = (0,3,9)$ r.l.u., and the corresponding momentum resolution along L (Figure 3.8(b)). I then calculate the effect of the momentum resolution: Figure 3.8(c) shows the two-spinon excitation lower and upper boundaries as given by the model (Equation 3.3), while, in Figure 3.8(d), I show the effect of the finite momentum resolution. I note that the effect is large at the Brillouin zone center where the momentum resolution makes the lower-boundary of the two-spinon continuum look gapped.

In the next section, I will perform numerical simulations of the $S_{cc}(\mathbf{q},\omega)$, including the effect of a finite momentum resolution, to extract the principal magnetic interactions in $CaIrO_3$.

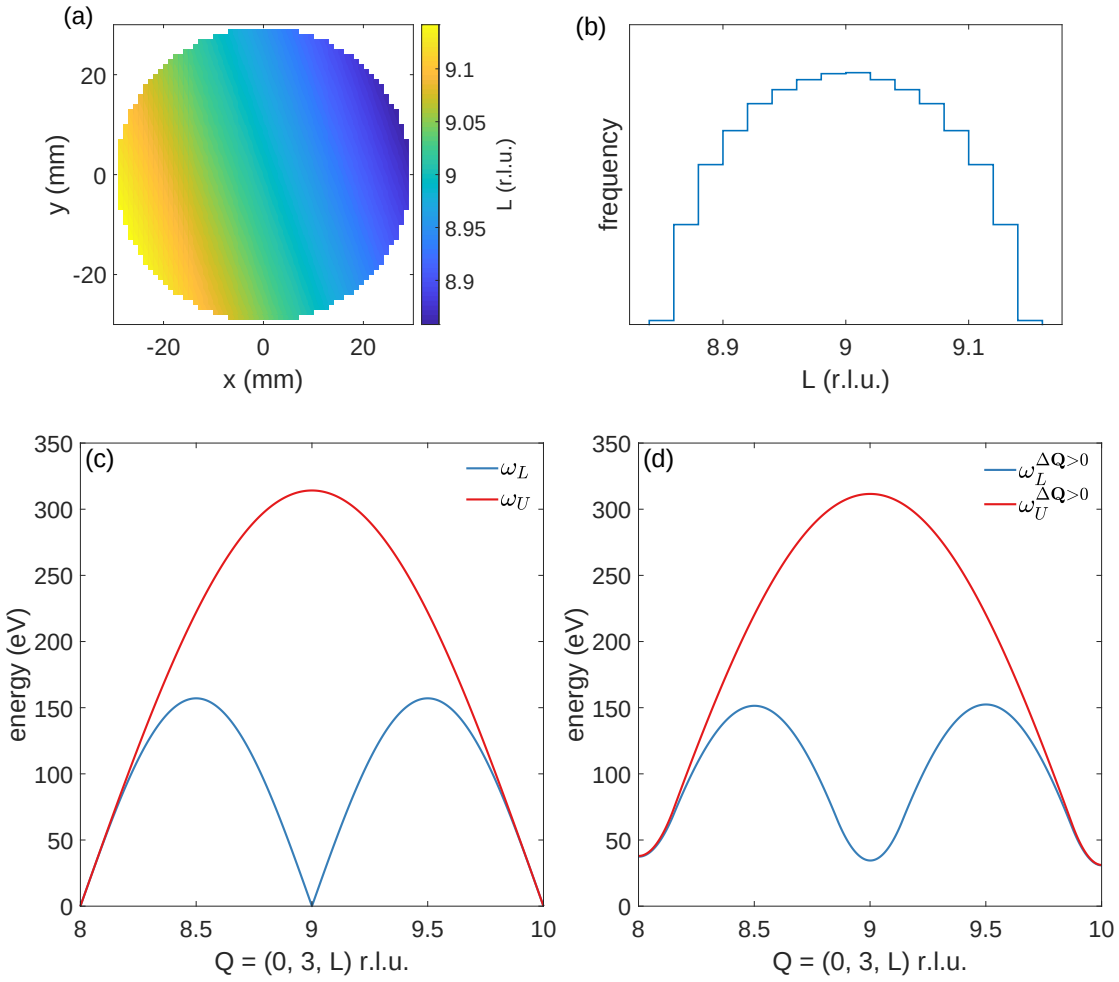

Figure 3.8: (a) Distribution of the values of the momentum transfer over the analyzer surface, nominally centered at momentum transfer $\mathbf{Q} = (0, 3, 9)$ r.l.u. in the case of analyzer diameter of 60 mm and sample to analyzer distance of 1 m. (b) Frequency of each momentum transfer value on the analyzer surface. (c) Two-parameters bounds reported in Equation 3.3 (ω_L in blue and ω_U in red). (d) Boundary curves of the two-spinon dynamic structure factor with the effect of finite momentum resolution of the analyzer (ω_L in blue and ω_U in red).

3.6 Optimization of the magnetic couplings

In order to extract the best estimate of the magnetic couplings, I systematically compare simulated and experimental spectra following the procedure below.

1. I simulate $S_{cc}(\mathbf{q}_i, \omega)$ for a set of $J_c > 0$ eV and $J_a < 0$ eV with realistic values of the experimental parameters at a specific momentum transfer $\mathbf{q}_i$ within the momentum resolution covered by the analyzer. Specifically, I:
   (a) evaluate $S_{uc}(\mathbf{q}_i, \omega)$ using Equation 3.4;
   (b) extract $\chi''_{uc}(\mathbf{q}_i, \omega)$ from $S_{uc}(\mathbf{q}_i, \omega)$ using Equation 3.6;
   (c) calculate $\chi'_{uc}(\mathbf{q}_i, \omega)$ using the Kramers-Kronig relations (KK) and determine $\chi_{uc}(\mathbf{q}_i, \omega)$ as $\chi_{uc}(\mathbf{q}_i, \omega) = \chi'_{uc}(\mathbf{q}_i, \omega) + i\chi''_{uc}(\mathbf{q}_i, \omega)$;

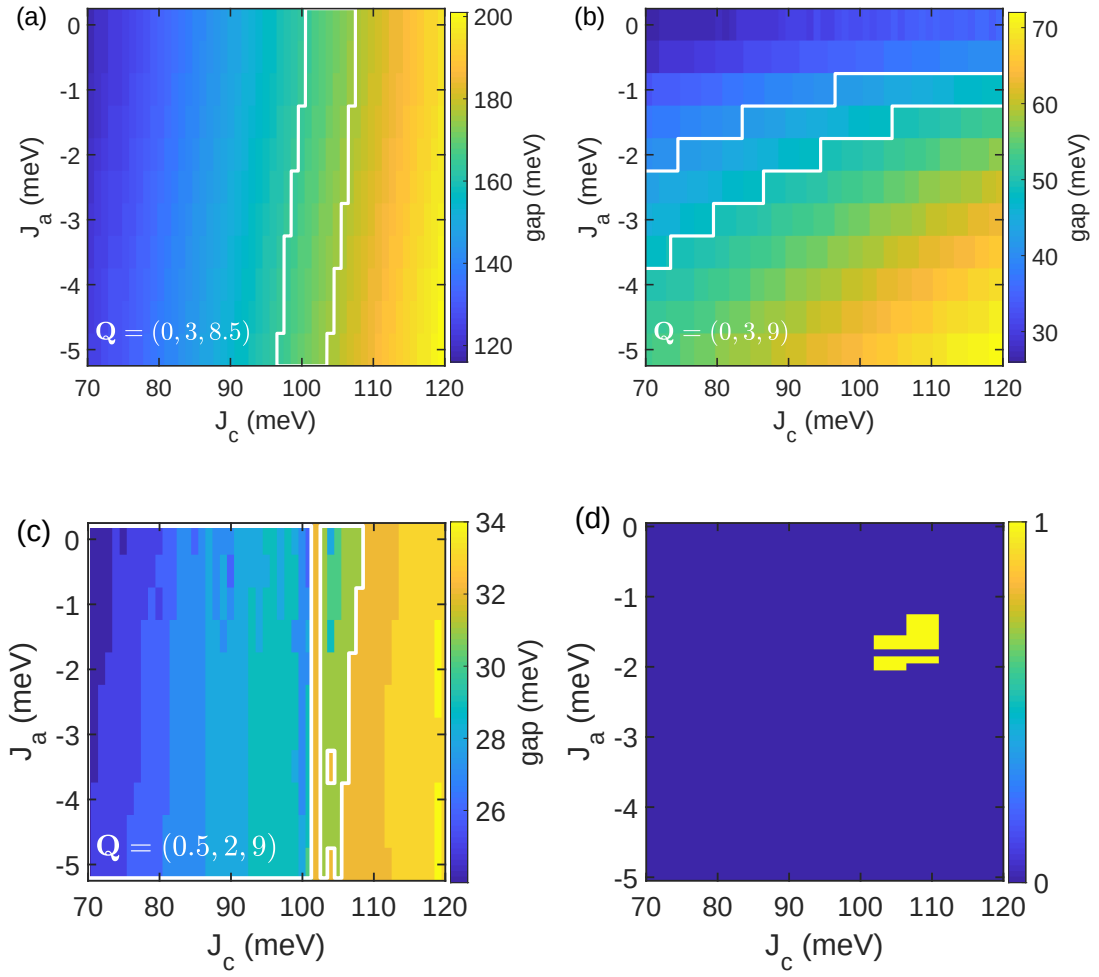

Figure 3.9: Maps of gap positions of $S_{cc}(\mathbf{q},\omega)$ in the (J_c, J_a) phase space at different transferred momenta: $\mathbf{Q} = (0, 3, 8.5)$ r.l.u. in panel (a), $\mathbf{Q} = (0, 3, 9)$ r.l.u. in panel (b) and $\mathbf{Q} = (0.5, 2, 9)$ r.l.u. in panel (c). In each map, areas within the white solid lines enclose (J_c, J_a) couples whose corresponding gaps are consistent with experimental ones. The resulting intersection of selected (J_c, J_a) couples is reported in panel (d).

(d) calculate $\chi_{cc}(\mathbf{q}_i,\omega)$ from $\chi_{uc}(\mathbf{q}_i,\omega)$ using Equation 3.5 and extract $\chi''_{cc}(\mathbf{q}_i,\omega)$;

(e) determine $S_{cc}(\mathbf{q}_i,\omega)$ using Equation 3.6.

The previous steps can be summarized in the following chain of operations

$$S_{uc}(\mathbf{q}_i,\omega) \xrightarrow{\text{Eq. 3.6}} \chi''_{uc}(\mathbf{q}_i,\omega) \xrightarrow{\text{KK}} \chi_{uc}(\mathbf{q}_i,\omega) \xrightarrow{\text{Eq. 3.5}} \chi_{cc}(\mathbf{q}_i,\omega) \xrightarrow{\text{Eq. 3.6}} S_{cc}(\mathbf{q}_i,\omega) \tag{3.7}$$

2. I simulate the measured RIXS spectrum $S_{cc}(\mathbf{q},\omega)$ by summing $S_{cc}(\mathbf{q}_i,\omega)$ over all the $\mathbf{q}_i$'s covered by the analyzer

$$S_{cc}(\mathbf{q},\omega) = \sum_{\mathbf{q}_i \in analyzer} S_{cc}(\mathbf{q}_i,\omega) \tag{3.8}$$

The values of the magnetic gaps of the simulated $S_{cc}(\mathbf{q},\omega)$ are mapped in Figure 3.9 for different values of the momentum transfer $\mathbf{Q} = (0, 3, 8.5)$ r.l.u. in panel (a), $\mathbf{Q} = (0, 3, 9)$ r.l.u. in panel (b) and $\mathbf{Q} = (0.5, 2, 9)$ in panel (c);

3. From the whole (J_c, J_a) phase space, I retain the values of the magnetic interactions that produce a gap consistent with the RIXS spectra at the three transferred momenta, within some uncertainty (see Figure 3.9(d)). In particular $\approx 170 \pm 5$ meV at $\mathbf{Q} = (0, 3, 8.5)$ r.l.u., $\approx 44.5 \pm 5$ meV at $\mathbf{Q} = (0, 3, 9)$ r.l.u. and $\approx 25.5 \pm 5$ meV at $\mathbf{Q} = (0.5, 2, 9)$ r.l.u. The corresponding areas are highlighted in Figure 3.9 by the white contours;

4. I compare the simulated $S_{cc}(\mathbf{q},\omega)$, convoluted by the energy resolution of the spectrometer, to the data and select the couple of $(\bar{J}_c, \bar{J}_a)$ that better reproduces the shape of the experimental spectra. In order to do that, I define a parameter
$$\Delta(J_c, J_a) = \min_c \|y_{exp} - c \cdot S_{cc}(\mathbf{q},\omega)\| \tag{3.9}$$
for the selected (J_c, J_a) couples that quantifies the overlap between experimental and simulated spectra. I then select $(\bar{J}_c, \bar{J}_a)$ such that
$$\Delta(\bar{J}_c, \bar{J}_a) \equiv \min_{J_c, J_a}\{\Delta^{\mathbf{Q}=(0,3,8.5)}(J_c, J_a) + \Delta^{\mathbf{Q}=(0,3,9)}(J_c, J_a) + \Delta^{\mathbf{Q}=(0.5,2,9)}(J_c, J_a)\} \tag{3.10}$$

The best-fit couple is $(\bar{J}_c, \bar{J}_a) = (100, -1.5)$ meV and produces gaps of 166, 47 and 28 meV at $\mathbf{Q} = (0, 3, 8.5)$, $\mathbf{Q} = (0, 3, 9)$ and $\mathbf{Q} = (0.5, 2, 9)$ r.l.u., respectively. A comparison between the experimental spectra (red dashed lines) and $S_{cc}(\mathbf{q},\omega)$ (blue solid lines) at the three transferred momenta is reported in Figure 3.10 ($\mathbf{Q} = (0, 3, 8.5$ r.l.u. in panel (a), $\mathbf{Q} = (0, 3, 9)$ r.l.u. in panel (b) and $\mathbf{Q} = (0.5, 2, 9)$ r.l.u. in panel (c)). In order to highlight the effect of the finite momentum resolution and of the coupling between the chains, I report the simulated spin dynamic structure factors for $J_a = 0$ and finite momentum resolution (green dotted lines), $J_a = \bar{J}_a$ and $\Delta\mathbf{q} = 0$ (purple dotted lines) and $J_a = 0$ and $\Delta\mathbf{q} = 0$ (orange dotted lines). At $\mathbf{Q} = (0, 3, 8.5)$ r.l.u. the effect of both J_a and $\Delta\mathbf{q}$ is not so evident, At $\mathbf{Q} = (0, 3, 9)$ r.l.u. the effect of momentum resolution and the coupling between the chains are more pronounced. Indeed, the orange curve ($J_a = 0$ and $\Delta\mathbf{q} = 0$) is practically gapless and so is the green curve ($J_a = \bar{J}_a$), but with a more asymmetric shape. The opening of the gap, instead, is mostly due to the finite momentum resolution alone. Finally, at $\mathbf{Q} = (0.5, 2, 9)$ r.l.u., J_a has no effect, as can be seen from Equation 3.5 with $q_x = \pi/2$, in which case $\chi_{cc}(\mathbf{q},\omega) = \chi_{uc}(\mathbf{q},\omega)$.

In Figure 3.11, I compare the full dispersion along the three principal directions in the sample reciprocal space as measured by RIXS (panels (a), (b) and (c)) and as simulated (panels (d), (e) and (f)) for $(\bar{J}_c, \bar{J}_a)$ at the actual experimental resolution. I note that the main experimental features are well reproduced by the simulations, including the small dispersion in the edge-sharing H direction and the two-spinon like continuum along the corner-sharing H direction. In addiction, the values obtained for $(\bar{J}_c, \bar{J}_a)$ are consistent with the results of *ab initio* quantum chemical calculations by Bogdanov et al.[66], who predicted an AFM coupling of 121 meV along the corner-sharing direction and a FM coupling of -7 meV along the edge-sharing direction.

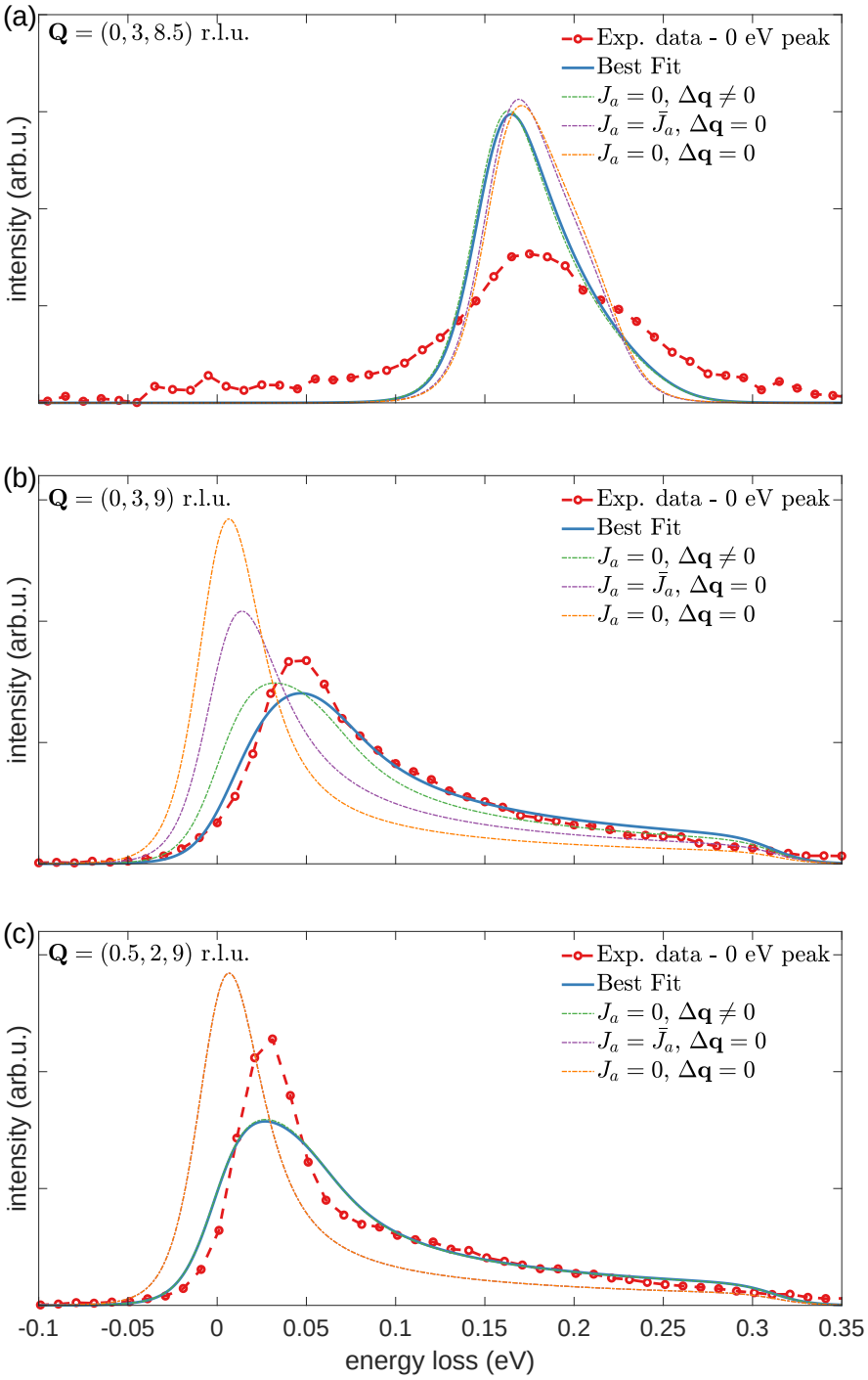

Figure 3.10: Comparisons between experimental data (red dashed lines) and spin dynamical structure factor of coupled chains $S_{cc}(\mathbf{q}, \omega)$ with $J_a = 0$ and $\Delta\mathbf{q} = 0$ (orange dotted lines), with $J_a = \bar{J}_a$ and $\Delta\mathbf{q} = 0$ (purple dotted lines), with $J_a = 0$ and $\Delta\mathbf{q} \neq 0$ only (green dotted lines), with both $J_a = \bar{J}_a$ and $\Delta\mathbf{q} \neq 0$ (blue solid lines). Different panels refer to different transferred momenta: $\mathbf{Q} = (0, 3, 8.5)$ r.l.u. in panel (a), $\mathbf{Q} = (0, 3, 9)$ r.l.u. in panel (b) and $\mathbf{Q} = (0.5, 2, 9)$ r.l.u. in panel (c).

However, we cannot expect that this model captures entirely the experimental observations, in that many approximations are introduced. In particular:

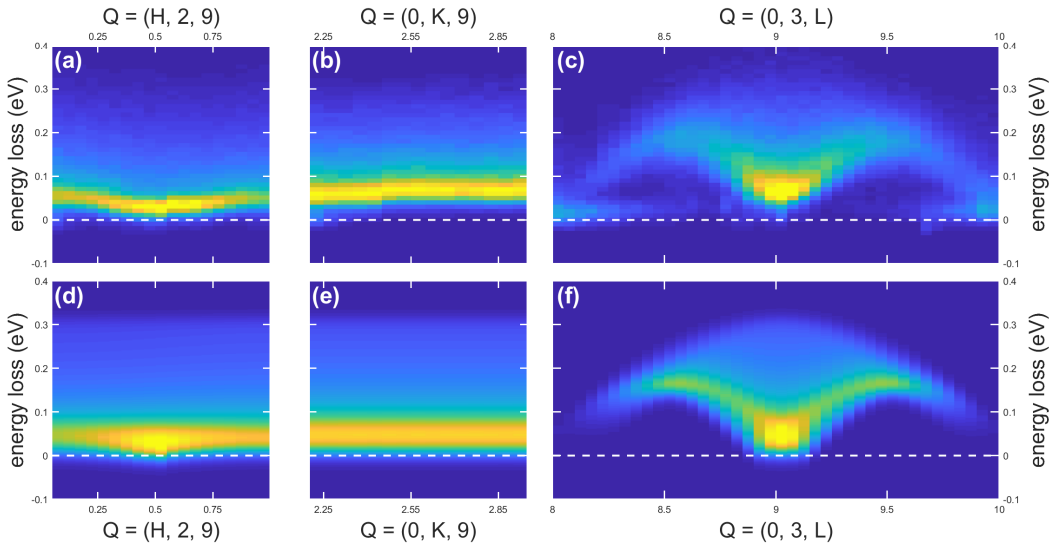

Figure 3.11: Panels (a), (b) and (c) report RIXS experimental spectra along H, K and L directions, respectively. Panels (d), (e) and (f) show the two-spinon dynamic structure factor of coupled spin chains $S_{cc}(\mathbf{q}, \omega)$ with $(\bar{J}_c, \bar{J}_a) = (100, -1.5)$ meV along H, K and L directions, respectively.

- The Heisenberg model assumes isotropic magnetic interactions. We know, however, that the magnetism of $CaIrO_3$ is certainly affected by anisotropies, including a weak Dzyaloshinskii-Moriya interaction that cants the magnetic moments away from collinearity[8]. Magnetic anisotropies are likely correlated with the large tetragonal crystal field splitting of the electronic states as observed by Moretti Sala et al.[10];

- The magnetic dynamics of the Heisenberg spin chain includes higher-order excitations than the two-spinon continuum. In particular, it was estimated that the four-spinon excitations contribute to the full magnetic dynamic structure factor amounts to 27 %, i.e. a sizable fraction of the two-spinon continuum. Since an analytical solution for the magnetic dynamic structure factor exists only for the two-spinon excitations, I decided not to complicate the calculation of $S_{uc}(\mathbf{q}, \omega)$ by excluding higher-order excitations;

- Finally, it is not obvious that the dynamic structure factor can be compared to the RIXS cross section. This is the subject of an ongoing debate[47].

Given the limitations listed above, I believe that the agreement between experimental and simulated spectra is satisfactory, meaning that the simple Heisenberg model captures most of the physics of the magnetic excitations in $CaIrO_3$. Further targeted experiments and refinements of the theoretical model, however, might be beneficial to isolate the effect of minor magnetic couplings and gain deeper insight in the magnetism of $CaIrO_3$.

Conclusions

In the present thesis, I focus on the magnetic dynamics of $CaIrO_3$ as measured by RIXS. $CaIrO_3$ is an interesting compound: the presence of large SOC and the important tetragonal distortion of the octahedra highly alter the $j_{eff} = 1/2$ Mott insulating state, usually adopted to describe other iridates[10]. $CaIrO_3$ features both corner- and edge-sharing IrO_6 octahedra along the c and a axes, respectively. From theoretical predictions, magnetic interactions are predominantly AFM along the corner-sharing direction and FM along the edge-sharing direction[23], thus making $CaIrO_3$ a quasi-1D magnet. However, a direct experimental proof is lacking. Therefore, I carried out RIXS measurements of the magnetic dynamics of $CaIrO_3$ to estimate its principal magnetic interactions.

RIXS measurements have been performed at ID20, the hard x-ray RIXS beamline of the ESRF. The temperature dependence analysis of the low-energy excitations reveals that their intensity evolution is closely correlated to the Néel temperature. In particular, the temperature dependence of the quasi-elastic line resembles that of AC dynamic magnetic susceptibility measured by Gunasekera et al.[58], namely it is also strongly peaked at the magnetic transition temperature. RIXS spectra as a function of the momentum transfer show a strong evolution along the corner-sharing L direction, a weak dependence along the edge-sharing H direction and no dependence at all along the K direction. The profile of the low-energy excitations is similar to that of a two-spinon continuum, as reported in various systems[59,70], so I conclude that the magnetism of $CaIrO_3$ has mostly one dimensional character.

In order to extract quantitative information about the characteristic magnetic interaction in $CaIrO_3$, I adopt a simple model based on the 1D $s = 1/2$ Heisenberg spin chain, characterized by an isotropic magnetic interaction J_c between neighboring spins[67]. I introduce a finite coupling J_a between the magnetic chains within the RPA approximation and simulate the RIXS response by calculating the magnetic dynamic structure factor and by taking into account the finite energy and momentum resolution of the spectrometer[11,68].

By doing so, I extract values for the magnetic interactions that best described experimental data, following the procedure described in Section 3.6. I obtain $(\bar{J}_c, \bar{J}_a) = (100, -1.5)$ meV, consistent with *ab initio* quantum chemical calculations by Bogdanov et al.[66]. Despite the simplicity of the model, it nicely reproduces most of the features observed experimentally.

Further improvements in the understanding of the magnetic dynamics of $CaIrO_3$ may require in future experiments with better energy and momentum resolution. Alternatively, one could perform RIXS experiments with polarization analysis of the scattered radiation, which imposes additional constraints on the excitations

visible in the RIXS process. Work in this direction is in progress.

Appendix A

The $\mathcal{UB}$ matrix formalism and the calculation of momentum resolution

In this Appendix, I will introduce the $\mathcal{UB}$ matrix formalism used to estimate the finite momentum resolution of the ID20 spectrometer. In my analysis, I will follow the work of Moretti Sala et al.[11].

As already said in Section 2.4.2, the calculation of the momentum resolution requires the knowledge of $\mathcal{U}$ and $\mathcal{B}$ matrices. The former connects the sample and the laboratory reference frames. The latter defines a Cartesian reference frame in the sample reciprocal space and so it depends on lattice constants. Using the formalism of Busing and Levy[71], $\mathcal{B}$ is given by

$$\mathcal{B} = \begin{pmatrix} a^* & b^*\cos(\gamma^*) & c^*\cos(\beta^*) \\ 0 & b^*\sin(\gamma^*) & -c^*\sin(\beta^*)\cos(\alpha) \\ 0 & 0 & 1/c \end{pmatrix} \tag{A.1}$$

The momentum transfer defined in Equation 2.10 depends also on $\mathcal{U}$. In order to find it, the following method has to be followed: we have to experimentally find two non-collinear Bragg reflections and use them to derive the relative sample orientation with respect to the laboratory frame. So ideally, given two Bragg reflections expressed in the sample reciprocal space $\mathbf{q}_1^{hkl}$, $\mathbf{q}_2^{hkl}$, the following relation

$$\begin{aligned} \mathbf{q}_1^{hkl} &= (\mathcal{T}_1^{\omega\chi\varphi}\mathcal{UB})^{-1}\,\mathbf{q}_1^{2\vartheta} \\ \mathbf{q}_2^{hkl} &= (\mathcal{T}_2^{\omega\chi\varphi}\mathcal{UB})^{-1}\,\mathbf{q}_2^{2\vartheta} \end{aligned} \tag{A.2}$$

holds, where $\mathcal{T}_1^{\omega\chi\varphi}$ ($\mathcal{T}_2^{\omega\chi\varphi}$) and $\mathbf{q}_1^{2\vartheta}$ ($\mathbf{q}_2^{2\vartheta}$) contain information about the scattering geometry and the sample angles corresponding to the first and the second Bragg reflections. Due to uncertainties on angle measurements and/or lattice constants, it is not possible to find an orthogonal matrix $\mathcal{U}$ that satisfies both the previous identities. So the method proposed by Busing and Levy[71] is to require that $\mathbf{q}_1^{hkl}$ must be parallel to $\mathbf{q}_1^{2\vartheta}$ and $\mathbf{q}_2^{hkl}$ has to lie in the plane generated by $\mathbf{q}_1^{2\vartheta}$ and $\mathbf{q}_2^{2\vartheta}$. By defining

$$\begin{aligned} \mathbf{t}_1 &= \mathcal{B}\mathbf{q}_1^{hkl}, \\ \mathbf{t}_3 &= \mathcal{B}(\mathbf{q}_1^{hkl} \times \mathbf{q}_2^{hkl}), \\ \mathbf{t}_2 &= \mathbf{t}_1 \times \mathbf{t}_3, \end{aligned} \tag{A.3}$$

$$\begin{aligned}\mathbf{v}_1 &= \mathcal{T}_1^{\omega\chi\varphi^{-1}}\mathbf{q}_1^{2\vartheta},\\ \mathbf{v}_3 &= \mathcal{T}_1^{\omega\chi\varphi^{-1}}\mathbf{q}_1^{2\vartheta} \times \mathcal{T}_2^{\omega\chi\varphi^{-1}}\mathbf{q}_2^{2\vartheta},\\ \mathbf{v}_2 &= \mathbf{v}_1 \times \mathbf{v}_3,\end{aligned} \tag{A.4}$$

and so

$$\begin{aligned}\mathcal{T} &= (\mathbf{t}_1/|\mathbf{t}_1|, \mathbf{t}_2/|\mathbf{t}_2|, \mathbf{t}_3/|\mathbf{t}_3|),\\ \mathcal{V} &= (\mathbf{v}_1/|\mathbf{v}_1|, \mathbf{v}_2/|\mathbf{v}_2|, \mathbf{v}_3/|\mathbf{v}_3|),\end{aligned} \tag{A.5}$$

then the $\mathcal{U}$ matrix can be found as

$$\mathcal{U} = \mathcal{V}\mathcal{T}^{-1}. \tag{A.6}$$

Finally, given the $\mathcal{U}$ and $\mathcal{B}$ matrices, the sample (ω, χ and φ) and the spectrometer (γ and δ) angles, one can project $\mathbf{q}^{2\vartheta}$ into the sample reciprocal space $\mathbf{q}^{hkl}$, using Equation A.2.

The momentum resolution is related to the uncertainties on the scattering arm angles, $\Delta\gamma$ and $\Delta\delta$, due to the finite aperture of the analyzer, A. The finite momentum resolution in the sample reciprocal space can be expressed as

$$\Delta\mathbf{q}^{hkl} \simeq (\mathcal{T}^{\omega\chi\varphi}\mathcal{UB})^{-1}\left(\frac{\partial\mathbf{q}^{2\vartheta}}{\partial\gamma}\Delta\gamma + \frac{\partial\mathbf{q}^{2\vartheta}}{\partial\delta}\Delta\delta\right), \tag{A.7}$$

where both $\Delta\gamma$ and $\Delta\delta$ are of the order of $A/|A|$ if $A \ll |A|$. If we assume that the scattering is quasi-elastic, so that $\lambda_o \simeq \lambda_i \simeq \lambda$, the previous equation becomes

$$\Delta\mathbf{q}^{hkl} \simeq (\mathcal{T}^{\omega\chi\varphi}\mathcal{UB})^{-1}\mathcal{T}^{2\vartheta}\mathbf{q}^{2\vartheta}, \tag{A.8}$$

that is the finite momentum resolution of the spectrometer.

Appendix B

Fit of $CaIrO_3$ RIXS spectra with Pearson VII functions

In this Appendix, I will explain the computational method used to fit RIXS spectra of $CaIrO_3$. The principle I followed writing the fit program is the Occam's razor: the best fit is characterized by the lowest possible number of curves, each one associated to a well defined physical phenomenon. The importance of the fit resides in one particular aspect: the sizes of magnetic gap, used as fixed parameters to extract the mangetic couplings in Section 3.6, correspond to the positions of the fit functions.

The Pearson VII function is chosen to shape the experimental features. This function belongs to the family of continuous probability distributions developed by Pearson[72] in 1916. In particular, the Pearson VII represents a continuous modulation from a Gaussian to a Lorentzian extreme[73]. Its analytic expression is given by

$$I(x)_{PVII} = I_{max} \cdot \left[1 + \left(2^{1/\mu} - 1\right) \cdot \left(\frac{2\,(x - x_0)}{\Gamma}\right)^2\right]^{-\mu}, \tag{B.1}$$

where x_0 is its position, Γ is its full width at half maximum (FWHM) and μ is the modulation parameter that control the *gaussiniaty* (or *lorentzianity*) of the Pearson VII curve: $\mu = 1$ yields to Lorentz function, whereas $\mu = \infty$ leads to Gaussian shape.

The energy resolution of a RIXS experiment is experimentally determined by collecting a pure elastic line and extracting its width. Such value will remain as a lower bound for all the subsequent spectra. The maximum value of the coefficient μ is also fixed to that of the elastic peak, since all spectral feature will be *more Lorentzian* than the elastic line due to the finite lifetime of the intermediate state. In Figure B.1, it is reported the elastic peak collected at ID20 at ESRF (blue solid line). The Pearson VII fit is also shown (red solid line).

I now investigate a generic RIXS spectrum of $CaIrO_3$. In Figure B.2, I report the spectrum recorded at the momentum transfer $\mathbf{Q} = (0, 3, 9)$ r.l.u. at $T = 40$ K. Raw data are plotted with black circled line and the red line is the total fit function, equal to the sum of all curves described hereafter. The quasi-elastic line is forced to be close to 0 eV energy loss and its width c and μ coefficient are fixed to the values obtained before. The two curves labeled by β_1 and β_2 are related

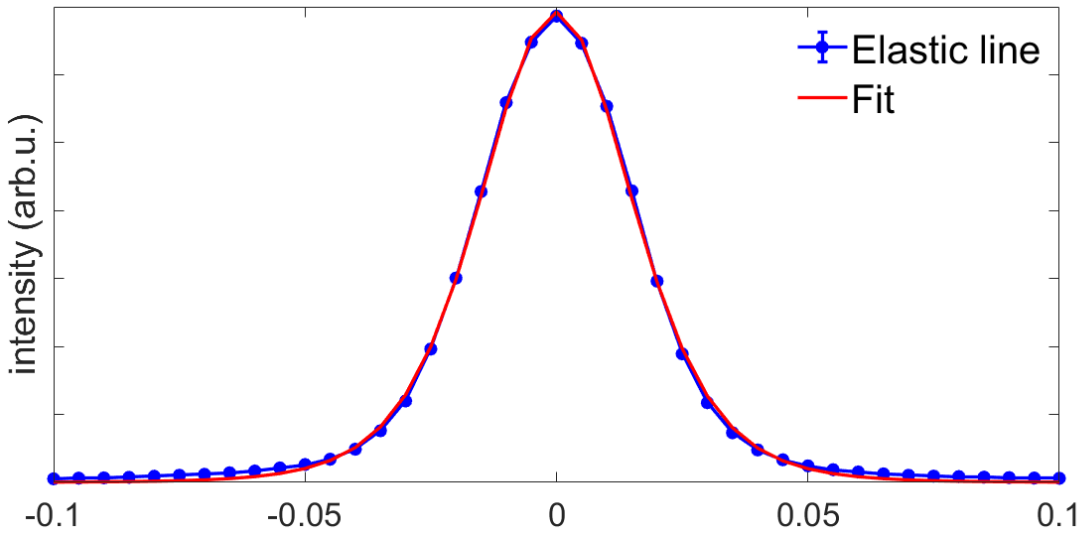

Figure B.1: The elastic line collected at ID20 at ESRF (blue solid line) is fitted with a Pearson VII function. The values extracted from the fit are $\mu \approx 3.64$ and $c \approx 36$ meV.

to magnetic excitations in the material (see Section 3.3). It can be seen that the intensity profile under 0.35 eV is manifestly asymmetric towards higher energies. So β_1 is fitted with a symmetric Pearson VII function, while β_2 is fitted by a strongly asymmetric Pearson VII and is defined as

$$\beta_2(x) = \begin{cases} I_{max} \cdot \left[1 + \left(2^{1/\mu} - 1\right) \cdot \left(\frac{2(x-x_0)}{(\Gamma+\Psi_1)}\right)^2\right]^{-\mu}, & \text{if } x \leq x_0 \\ I_{max} \cdot \left[1 + \left(2^{1/\mu} - 1\right) \cdot \left(\frac{2(x-x_0)}{(\Gamma+\Psi_2)}\right)^2\right]^{-\mu}, & \text{if } x > x_0 \end{cases} \tag{B.2}$$

where Ψ_1 and Ψ_2 are left and right asymmetry respectively. At ≈ 0.4 eV, usually the intensity of RIXS spectra of $CaIrO_3$ shows a sudden increase. Furthermore, after both the δ_1 and δ_2 curves, the intensity does not go to zero. Due to these reasons, I assume the presence of a continuum of excitations modeled as the following sigmoid function

$$I_\sigma = I_{max} \frac{1}{1 + e^{-\alpha(x-x_0)}}, \tag{B.3}$$

where the α coefficient defines the slope of the initial ramp of the sigmoid and its upper bound is defined as $2(\ln\left(3 - 2\sqrt{2}\right))/c$. x_0 is the position of the sigmoid that is constrained to be equal to the position of the "exciton" ξ, since it coincides with the rapid increase of intensity. The exciton is located ≈ 0.42 eV. Its origin, as the nature of δ_1 and δ_2 feature, has been already discussed by Moretti Sala et al.[10]. ξ, δ_1 and δ_2 are all fitted with symmetric Pearson VII functions.

The goodness of the fit is evaluated using the coefficient of determination R^2. The fit process is divided in three steps:

1. the first fit is made by purely Gaussian curves and provide an initial set of starting points for the subsequent fits;

2. the second step is done with Pearsons, including also the sigmoid. Once again, starting points of the fit are adjusted;

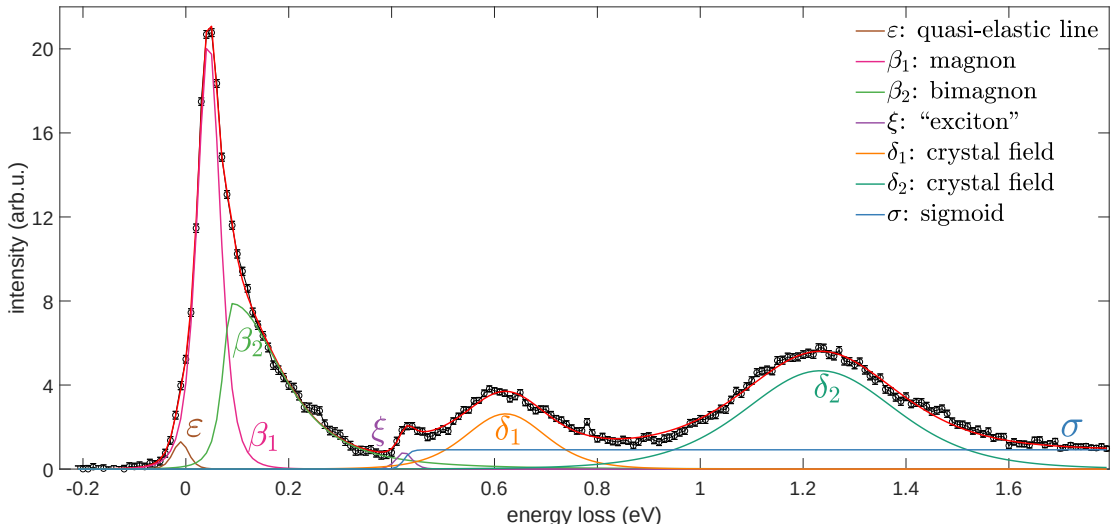

Figure B.2: RIXS spectrum of $CaIrO_3$ collected at momentum transfer $\mathbf{Q} = (0, 3, 9)$ r.l.u. and at $T = 40$ K (circled black line), reporting also the overall fit function (red solid line). The spectrum is fitted with 6 Pearson VII curves and one sigmoid (σ, light blue solid line). The brown solid line labeled by ε is the quasi-elastic line, the other curves below 0.35 eV β_1 (pink solid line) and β_2 (green solid line) are fitted with symmetric and asymmetric Pearson VII, respectively. The curve denoted by ξ is the debated "exciton" at ≈ 0.42 eV, while the last two Pearson VII functions reproduce transitions between crystal field split states.

3. last passage is identically to the previous one, but with a lower tolerance (of the order of 10^{-10}).

If the resulting coefficient of determination is larger than a certain value, usually fixed to $R^2 \gtrsim 0.98$, the fit is accepted. Otherwise, starting point, lower and upper bounds are manually changed and the three-step process is restarted.

Bibliography

[1] William Witczak-Krempa et al. "Correlated quantum phenomena in the strong spin-orbit regime". In: *Annu. Rev. Condens. Matter Phys.* 5.1 (2014), pp. 57–82. DOI: 10.1146/annurev-conmatphys-020911-125138. URL: https://doi.org/10.1146/annurev-conmatphys-020911-125138.

[2] B. Keimer et al. "From quantum matter to high-temperature superconductivity in copper oxides". In: *Nature* 518 (Feb. 2015). Review Article, pp. 179–186. DOI: 10.1038/nature14165.

[3] A. P. Ramirez. "Colossal magnetoresistance". In: *Journal of Physics: Condensed Matter* 9.39 (1997), p. 8171. ISSN: 0953-8984. DOI: 10.1088/0953-8984/9/39/005. URL: http://stacks.iop.org/0953-8984/9/i=39/a=005.

[4] J. Okamoto et al. "Symmetry of Multiferroicity in a Frustrated Magnet $TbMn_2O_5$". In: *Phys. Rev. Lett.* 98 (15 Apr. 2007), p. 157202. DOI: 10.1103/PhysRevLett.98.157202. URL: https://link.aps.org/doi/10.1103/PhysRevLett.98.157202.

[5] B. J. Kim et al. "Novel $J_{\text{eff}} = 1/2$ Mott State Induced by Relativistic Spin-Orbit Coupling in Sr_2IrO_4". In: *Phys. Rev. Lett.* 101 (7 Aug. 2008), p. 076402. DOI: 10.1103/PhysRevLett.101.076402. URL: https://link.aps.org/doi/10.1103/PhysRevLett.101.076402.

[6] Jungho Kim et al. "Large Spin-Wave Energy Gap in the Bilayer Iridate $Sr_3Ir_2O_7$: Evidence for Enhanced Dipolar Interactions Near the Mott Metal-Insulator Transition". In: *Phys. Rev. Lett.* 109 (15 Oct. 2012), p. 157402. DOI: 10.1103/PhysRevLett.109.157402. URL: https://link.aps.org/doi/10.1103/PhysRevLett.109.157402.

[7] Sae Hwan Chun et al. "Direct Evidence for Dominant Bond-directional Interactions in a Honeycomb Lattice Iridate Na_2IrO_3". In: *Nature Physics* 11.6 (2015), p. 462. DOI: 10.1038/nphys3322.

[8] K. Ohgushi et al. "Metal-insulator transition in $Ca_{1-x}Na_xIrO_3$ with post-perovskite structure". In: *Phys. Rev. B* 74 (24 Dec. 2006), p. 241104. DOI: 10.1103/PhysRevB.74.241104. URL: https://link.aps.org/doi/10.1103/PhysRevB.74.241104.

[9] Kenya Ohgushi et al. "Resonant X-ray Diffraction Study of the Strongly Spin-Orbit-Coupled Mott Insulator $CaIrO_3$". In: *Phys. Rev. Lett.* 110 (21 May 2013), p. 217212. DOI: 10.1103/PhysRevLett.110.217212. URL: https://link.aps.org/doi/10.1103/PhysRevLett.110.217212.

[10] M. Moretti Sala et al. "$CaIrO_3$: A Spin-Orbit Mott Insulator Beyond the $j_{\text{eff}} = 1/2$ Ground State". In: *Phys. Rev. Lett.* 112 (17 Apr. 2014), p. 176402. DOI: 10.1103/PhysRevLett.112.176402. URL: https://link.aps.org/doi/10.1103/PhysRevLett.112.176402.

[11] M. Moretti Sala et al. "A high-energy-resolution resonant inelastic X-ray scattering spectrometer at ID20 of the European Synchrotron Radiation Facility". In: *Journal of Synchrotron Radiation* 25.2 (Mar. 2018), pp. 580–591. DOI: 10.1107/S1600577518001200. URL: https://doi.org/10.1107/S1600577518001200.

[12] W. D. Ryden, A. W. Lawson, and Carl C. Sartain. "Electrical Transport Properties of IrO_2 and RuO_2". In: *Phys. Rev. B* 1 (4 Feb. 1970), pp. 1494–1500. DOI: 10.1103/PhysRevB.1.1494. URL: https://link.aps.org/doi/10.1103/PhysRevB.1.1494.

[13] P.A. Cox. *Transition Metal Oxides: An Introduction to Their Electronic Structure and Properties*. International series of monographs on chemistry. OUP Oxford, 2010. ISBN: 9780199588947. URL: https://books.google.it/books?id=DdcUDAAAQBAJ.

[14] M. K. Crawford et al. "Structural and magnetic studies of Sr_2IrO_4". In: *Phys. Rev. B* 49 (13 Apr. 1994), pp. 9198–9201. DOI: 10.1103/PhysRevB.49.9198. URL: https://link.aps.org/doi/10.1103/PhysRevB.49.9198.

[15] G. Cao et al. "Anomalous magnetic and transport behavior in the magnetic insulator $Sr_3Ir_2O_7$". In: *Phys. Rev. B* 66 (21 Dec. 2002), p. 214412. DOI: 10.1103/PhysRevB.66.214412. URL: https://link.aps.org/doi/10.1103/PhysRevB.66.214412.

[16] Yogesh Singh and P. Gegenwart. "Antiferromagnetic Mott insulating state in single crystals of the honeycomb lattice material Na_2IrO_3". In: *Phys. Rev. B* 82 (6 Aug. 2010), p. 064412. DOI: 10.1103/PhysRevB.82.064412. URL: https://link.aps.org/doi/10.1103/PhysRevB.82.064412.

[17] Stuart Calder et al. "Magnetically driven metal-insulator transition in $NaOsO_3$". In: *Physical review letters* 108.25 (2012), p. 257209. DOI: 10.1103/PhysRevLett.108.257209.

[18] Zheng Ping et al. "Continuous magnetic phase transition in half-frustrated $Ca_2Os_2O_7$". In: *Physical Review B* 86 (Oct. 2012). DOI: 10.1103/PhysRevB.86.195108.

[19] David Griffiths. *Introduction of Quantum Mechanics*. Prentice Hall, Inc., 1995.

[20] K. V. Shanavas, Z. S. Popović, and S. Satpathy. "Theoretical model for Rashba spin-orbit interaction in d electrons". In: *Phys. Rev. B* 90 (16 Oct. 2014), p. 165108. DOI: 10.1103/PhysRevB.90.165108. URL: https://link.aps.org/doi/10.1103/PhysRevB.90.165108.

[21] Luuk J. P. Ament, Giniyat Khaliullin, and Jeroen Brink. "Theory of resonant inelastic x-ray scattering in iridium oxide compounds: Probing spin-orbit-entangled ground states and excitations". In: *Physical Review B* 84 (July 2011). DOI: 10.1103/PhysRevB.84.020403.

[22] S. J. Moon et al. "Electronic structures of layered perovskite Sr_2MO_4 (M = Ru, Rh, and Ir)". In: *Phys. Rev. B* 74 (11 Sept. 2006), p. 113104. DOI: 10.1103/PhysRevB.74.113104. URL: https://link.aps.org/doi/10.1103/PhysRevB.74.113104.

[23] G. Jackeli and G. Khaliullin. "Mott Insulators in the Strong Spin-Orbit Coupling Limit: From Heisenberg to a Quantum Compass and Kitaev Models". In: *Phys. Rev. Lett.* 102 (1 Jan. 2009), p. 017205. DOI: 10.1103/PhysRevLett.102.017205. URL: https://link.aps.org/doi/10.1103/PhysRevLett.102.017205.

[24] Matteo Rossi. "Resonant inelastic X-ray scattering on spin-orbit-induced correlated-electron systems : scientific applications and instrumental developments". Theses. Université Grenoble Alpes, Dec. 2017. URL: https://tel.archives-ouvertes.fr/tel-01799557.

[25] C David Martin et al. "High-pressure structure and bonding in $CaIrO_3$: The structure model of $MgSiO_3$ post-perovskite investigated with time-of-flight neutron powder diffraction". In: *American Mineralogist* 92 (Nov. 2007). DOI: 10.2138/am.2007.2585.

[26] Ken Niwa et al. "Lattice preferred orientation in $CaIrO_3$ perovskite and post-perovskite formed by plastic deformation under pressure". In: *Physics and Chemistry of Minerals* 34 (Jan. 2007), pp. 679–686. DOI: 10.1007/s00269-007-0182-6.

[27] J.-G. Cheng et al. "High-pressure synthesis and physical properties of perovskite and post-perovskite $Ca_{1-x}Sr_xIrO_3$". In: *Phys. Rev. B* 83 (6 Feb. 2011), p. 064401. DOI: 10.1103/PhysRevB.83.064401. URL: https://link.aps.org/doi/10.1103/PhysRevB.83.064401.

[28] B. J. Kim et al. "Phase-Sensitive Observation of a Spin-Orbital Mott State in Sr_2IrO_4". In: *Science* 323.5919 (2009), pp. 1329–1332. ISSN: 0036-8075. DOI: 10.1126/science.1167106. eprint: http://science.sciencemag.org/content/323/5919/1329.full.pdf. URL: http://science.sciencemag.org/content/323/5919/1329.

[29] Stefano Boseggia et al. "Locking of iridium magnetic moments to the correlated rotation of oxygen octahedra in Sr_2IrO_4 revealed by x-ray resonant scattering". In: *Journal of physics. Condensed matter : an Institute of Physics journal* 25 (Sept. 2013), p. 422202. DOI: 10.1088/0953-8984/25/42/422202.

[30] S Boseggia et al. "On the magnetic structure of $Sr_3Ir_2O_7$: an x-ray resonant scattering study". In: *Journal of Physics: Condensed Matter* 24.31 (July 2012), p. 312202. DOI: 10.1088/0953-8984/24/31/312202. URL: https://doi.org/10.1088%2F0953-8984%2F24%2F31%2F312202.

[31] S. Boseggia et al. "Antiferromagnetic order and domains in $Sr_3Ir_2O_7$ probed by x-ray resonant scattering". In: *Phys. Rev. B* 85 (18 May 2012), p. 184432. DOI: 10.1103/PhysRevB.85.184432. URL: https://link.aps.org/doi/10.1103/PhysRevB.85.184432.

[32] H. Okabe et al. "Ba_2IrO_4: A spin-orbit Mott insulating quasi-two-dimensional antiferromagnet". In: *Phys. Rev. B* 83 (15 Apr. 2011), p. 155118. DOI: 10.1103/PhysRevB.83.155118. URL: https://link.aps.org/doi/10.1103/PhysRevB.83.155118.

[33] S. Boseggia et al. "Robustness of Basal-Plane Antiferromagnetic Order and the J_{eff}=1/2 State in Single-Layer Iridate Spin-Orbit Mott Insulators". In: *Phys. Rev. Lett.* 110 (11 Mar. 2013), p. 117207. DOI: 10.1103/PhysRevLett.110.117207. URL: https://link.aps.org/doi/10.1103/PhysRevLett.110.117207.

[34] Zohar Nussinov and Jeroen van den Brink. "Compass models: Theory and physical motivations". In: *Rev. Mod. Phys.* 87 (1 Jan. 2015), pp. 1–59. DOI: 10.1103/RevModPhys.87.1. URL: https://link.aps.org/doi/10.1103/RevModPhys.87.1.

[35] Alexei Kitaev. "Anyons in an exactly solved model and beyond". In: *Annals of Physics* 321.1 (2006). January Special Issue, pp. 2–111. ISSN: 0003-4916. DOI: https://doi.org/10.1016/j.aop.2005.10.005. URL: http://www.sciencedirect.com/science/article/pii/S0003491605002381.

[36] Y. Miura et al. "New-Type Phase Transition of Li_2RuO_3 with Honeycomb Structure". In: *Journal of the Physical Society of Japan* 76.3 (Mar. 2007), p. 033705. DOI: 10.1143/JPSJ.76.033705. eprint: cond-mat/0612026.

[37] Shigeto Hirai et al. "The crystal structure of $CaIrO_3$ post-perovskite revisited". In: *Zeitschrift für Kristallographie* 224.7 (Jan. 2009). DOI: 10.1524/zkri.2009.1138. URL: https://doi.org/10.1524/zkri.2009.1138.

[38] Hongbin Zhang, Kristjan Haule, and David Vanderbilt. "Effective J=1/2 Insulating State in Ruddlesden-Popper Iridates: An LDA+DMFT Study". In: *Phys. Rev. Lett.* 111 (24 Dec. 2013), p. 246402. DOI: 10.1103/PhysRevLett.111.246402. URL: https://link.aps.org/doi/10.1103/PhysRevLett.111.246402.

[39] W. Schülke. *Electron Dynamics by Inelastic X-Ray Scattering*. Oxford Science Publications. OUP Oxford, 2007. ISBN: 9780198510178. URL: https://books.google.it/books?id=EXwSDAAAQBAJ.

[40] Luuk J. P. Ament et al. "Resonant inelastic x-ray scattering studies of elementary excitations". In: *Rev. Mod. Phys.* 83 (2 June 2011), pp. 705–767. DOI: 10.1103/RevModPhys.83.705. URL: https://link.aps.org/doi/10.1103/RevModPhys.83.705.

[41] Robert J. Birgeneau et al. "Magnetic neutron scattering in hole-doped cuprate superconductors". In: *Journal of the Physical Society of Japan* 75.11 (2006), p. 111003. DOI: 10.1143/JPSJ.75.111003. URL: https://doi.org/10.1143/JPSJ.75.111003.

[42] S. K. Choi et al. "Spin Waves and Revised Crystal Structure of Honeycomb Iridate Na_2IrO_3". In: *Phys. Rev. Lett.* 108 (12 Mar. 2012), p. 127204. DOI: 10.1103/PhysRevLett.108.127204. URL: https://link.aps.org/doi/10.1103/PhysRevLett.108.127204.

[43] J Schlappa et al. "Spin–orbital separation in the quasi-one-dimensional Mott insulator Sr_2CuO_3". In: *Nature* 485.7396 (2012), p. 82. DOI: 10.1038/nature10974.

[44] C. Ulrich et al. "Momentum Dependence of Orbital Excitations in Mott-Insulating Titanates". In: *Phys. Rev. Lett.* 103 (10 Sept. 2009), p. 107205. DOI: 10.1103/PhysRevLett.103.107205. URL: https://link.aps.org/doi/10.1103/PhysRevLett.103.107205.

[45] L. Braicovich et al. "Magnetic Excitations and Phase Separation in the Underdoped $La_{2-x}Sr_xCuO_4$ Superconductor Measured by Resonant Inelastic X-Ray Scattering". In: *Phys. Rev. Lett.* 104 (7 Feb. 2010), p. 077002. DOI: 10.1103/PhysRevLett.104.077002. URL: https://link.aps.org/doi/10.1103/PhysRevLett.104.077002.

[46] L. Braicovich et al. "Momentum and polarization dependence of single-magnon spectral weight for Cu L_3-edge resonant inelastic x-ray scattering from layered cuprates". In: *Phys. Rev. B* 81 (17 May 2010), p. 174533. DOI: 10.1103/PhysRevB.81.174533. URL: https://link.aps.org/doi/10.1103/PhysRevB.81.174533.

[47] Chunjing Jia et al. "Persistent spin excitations in doped antiferromagnets revealed by resonant inelastic light scattering". In: *Nature communications* 5 (Feb. 2014), p. 3314. DOI: 10.1038/ncomms4314.

[48] M. W. Haverkort. "Theory of Resonant Inelastic X-Ray Scattering by Collective Magnetic Excitations". In: *Phys. Rev. Lett.* 105 (16 Oct. 2010), p. 167404. DOI: 10.1103/PhysRevLett.105.167404. URL: https://link.aps.org/doi/10.1103/PhysRevLett.105.167404.

[49] Matthieu Le Tacon et al. "Intense paramagnon excitations in a large family of high-temperature superconductors". In: *Nature Physics* 7 (July 2011), pp. 725–730. DOI: 10.1038/nphys2041.

[50] J. Als-Nielsen and D. McMorrow. *Elements of Modern X-ray Physics*. Wiley, 2011. ISBN: 9781119970156. URL: https://books.google.fr/books?id=rlqlboWlTRMC.

[51] Boris W. Batterman and Henderson Cole. "Dynamical Diffraction of X Rays by Perfect Crystals". In: *Rev. Mod. Phys.* 36 (3 July 1964), pp. 681–717. DOI: 10.1103/RevModPhys.36.681. URL: https://link.aps.org/doi/10.1103/RevModPhys.36.681.

[52] André Authier. "Dynamical theory of X-ray diffraction". In: *International Tables for Crystallography* (2006), pp. 626–646.

[53] S. Huotari et al. "Resonant inelastic hard x-ray scattering with diced analyzer crystals and position-sensitive detectors". In: *Review of Scientific Instruments* 77.5 (2006), p. 053102. DOI: 10.1063/1.2198805. eprint: https://doi.org/10.1063/1.2198805. URL: https://doi.org/10.1063/1.2198805.

[54] C Ponchut et al. "MAXIPIX, a fast readout photon-counting X-ray area detector for synchrotron applications". In: *Journal of Instrumentation* 6.01 (Jan. 2011), pp. C01069–C01069. DOI: 10.1088/1748-0221/6/01/c01069. URL: https://doi.org/10.1088%2F1748-0221%2F6%2F01%2Fc01069.

[55] H. Gretarsson et al. "Crystal-Field Splitting and Correlation Effect on the Electronic Structure of A_2IrO_3". In: *Phys. Rev. Lett.* 110 (7 Feb. 2013), p. 076402. DOI: 10.1103/PhysRevLett.110.076402. URL: https://link.aps.org/doi/10.1103/PhysRevLett.110.076402.

[56] Beom Hyun Kim, G. Khaliullin, and B. I. Min. "Electronic excitations in the edge-shared relativistic Mott insulator: Na_2IrO_3". In: *Phys. Rev. B* 89 (8 Feb. 2014), p. 081109. DOI: 10.1103/PhysRevB.89.081109. URL: https://link.aps.org/doi/10.1103/PhysRevB.89.081109.

[57] Ekaterina M. Plotnikova et al. "Jahn-Teller Effect in Systems with Strong On-Site Spin-Orbit Coupling". In: *Phys. Rev. Lett.* 116 (10 Mar. 2016), p. 106401. DOI: 10.1103/PhysRevLett.116.106401. URL: https://link.aps.org/doi/10.1103/PhysRevLett.116.106401.

[58] J Gunasekera et al. "Mott insulator-to-metal transition in yttrium-doped CaIrO3". In: *Journal of Physics: Condensed Matter* 27.5 (Jan. 2015), p. 052201. DOI: 10.1088/0953-8984/27/5/052201. URL: https://doi.org/10.1088%2F0953-8984%2F27%2F5%2F052201.

[59] Martin Mourigal et al. "Fractional spinon excitations in the quantum Heisenberg antiferromagnetic chain". In: *Nature Physics* 9.7 (2013), p. 435. DOI: 10.1038/nphys2652.

[60] Jean-Sébastien Caux, Jorn Mossel, and Isaac Pérez Castillo. "The two-spinon transverse structure factor of the gapped Heisenberg antiferromagnetic chain". In: *Journal of Statistical Mechanics: Theory and Experiment* 2008.08 (Aug. 2008), P08006. DOI: 10.1088/1742-5468/2008/08/p08006. URL: https://doi.org/10.1088%2F1742-5468%2F2008%2F08%2Fp08006.

[61] L.D. Faddeev and L.A. Takhtajan. "What is the spin of a spin wave?" In: *Physics Letters A* 85.6 (1981), pp. 375–377. ISSN: 0375-9601. DOI: https://doi.org/10.1016/0375-9601(81)90335-2. URL: http://www.sciencedirect.com/science/article/pii/0375960181903352.

[62] T. Giamarchi and Oxford University Press. *Quantum Physics in One Dimension*. International Series of Monographs on Physics. Clarendon Press, 2004. ISBN: 9780198525004. URL: https://books.google.it/books?id=1MwTDAAAQBAJ.

[63] Jean-Sébastien Caux and Rob Hagemans. "The four-spinon dynamical structure factor of the Heisenberg chain". In: *Journal of Statistical Mechanics: Theory and Experiment* 2006.12 (Dec. 2006), P12013–P12013. DOI: 10.1088/1742-5468/2006/12/p12013. URL: https://doi.org/10.1088%2F1742-5468%2F2006%2F12%2Fp12013.

[64] D. A. Tennant et al. "Unbound spinons in the S=1/2 antiferromagnetic chain $KCuF_3$". In: *Phys. Rev. Lett.* 70 (25 June 1993), pp. 4003–4006. DOI: 10.1103/PhysRevLett.70.4003. URL: https://link.aps.org/doi/10.1103/PhysRevLett.70.4003.

[65] M. Enderle et al. "Two-Spinon and Four-Spinon Continuum in a Frustrated Ferromagnetic Spin-1/2 Chain". In: *Phys. Rev. Lett.* 104 (23 June 2010), p. 237207. DOI: 10.1103/PhysRevLett.104.237207. URL: https://link.aps.org/doi/10.1103/PhysRevLett.104.237207.

[66] Nikolay A Bogdanov et al. "Post-perovskite CaIrO 3: A j= 1/2 quasi-one-dimensional antiferromagnet". In: *Physical Review B* 85.23 (2012), p. 235147. DOI: 10.1103/PhysRevB.85.235147.

[67] Gerhard Müller et al. "Quantum spin dynamics of the antiferromagnetic linear chain in zero and nonzero magnetic field". In: *Phys. Rev. B* 24 (3 Aug. 1981), pp. 1429–1467. DOI: 10.1103/PhysRevB.24.1429. URL: https://link.aps.org/doi/10.1103/PhysRevB.24.1429.

[68] Marc Bocquet et al. "Finite-temperature dynamical magnetic susceptibility of quasi-one-dimensional frustrated spin-$\frac{1}{2}$ Heisenberg antiferromagnets". In: *Phys. Rev. B* 64 (9 Aug. 2001), p. 094425. DOI: 10.1103/PhysRevB.64.094425. URL: https://link.aps.org/doi/10.1103/PhysRevB.64.094425.

[69] GJ Nilsen et al. "One-dimensional quantum magnetism in the anhydrous alum KTi(SO4)2". In: *New Journal of Physics* 17.11 (Nov. 2015), p. 113035. DOI: 10.1088/1367-2630/17/11/113035. URL: https://doi.org/10.1088%2F1367-2630%2F17%2F11%2F113035.

[70] J. C. Leiner et al. "Magnetic excitations of the Cu^{2+} quantum spin chain in Sr_3CuPtO_6". In: *Phys. Rev. B* 97 (10 Mar. 2018), p. 104426. DOI: 10.1103/PhysRevB.97.104426. URL: https://link.aps.org/doi/10.1103/PhysRevB.97.104426.

[71] W. R. Busing and H. A. Levy. "Angle calculations for 3- and 4-circle X-ray and neutron diffractometers". In: *Acta Crystallographica* 22.4 (Apr. 1967), pp. 457–464. DOI: 10.1107/S0365110X67000970. URL: https://doi.org/10.1107/S0365110X67000970.

[72] Karl Pearson. "Mathematical Contributions to the Theory of Evolution. XIX. Second Supplement to a Memoir on Skew Variation". In: *Philosophical Transactions of the Royal Society of London. Series A, Containing Papers of a Mathematical or Physical Character* 216 (1916), pp. 429–457. ISSN: 02643952. URL: http://www.jstor.org/stable/91092.

[73] Hejing Wang and Jian Zhou. "Numerical conversion between the Pearson VII and pseudo-Voigt functions". In: *Journal of applied crystallography* 38.5 (2005), pp. 830–832. DOI: 10.1107/S0021889805024490.

Acknowledgments

The first person to which I would express my gratitude is my supervisor, Prof. Marco Moretti. His passion and devotion inspired me from the very first time we met, but also during beamline nights watching spaghetti-westerns to keep ourselves awake. He taught me what it means to be an experimental scientist and how to deal with every problem in a positive and curious way. I had the privilege to work in the group of Prof. Giacomo Ghiringhelli, which I want to thank for it and for having always been an example for me. I cannot forget Prof. Lucio Braicovich, whose passion, but moreover his entire life, represent to me a continuous source of inspiration. I would like to thank also Matteo, Roberto and Riccardo for their patience and kindness to me. Thank you because your door was always open for me, for some questions about physics and for discussions about my possible future.

I am very grateful to my lab-mates, Benedetta, Mattia, Paolo and Leonardo who made very funny and pleasant my six-months thesis in the old RIXS laboratory at Politecnico di Milano. In particular, Benedetta, thank you for your kindness and optimism. Thank you Mattia for your passion for the unknown (as the unforgettable *"piccione"* problem) and a bit also for your *healthy* madness. I leave to you in inheritance the precious second monitor on my desk. Paolo, thank you not only for these six months in the lab, but for each moment in the last two years. Leonardo, the "youngest" student in the lab, you brought to us, but especially to me, a new vitality. I will always remember these months with you, mates, full of physics, talks about future perspective, but especially butter biscuits.

My thesis would have not been possible without the support of Politecnico di Milano and of the ESRF, where I performed my experiments. In particular, I would like to thank Dr. Emilie Lefrançois for allowing me to take part to her experiment and Dr. Mohamed Oudah, who partecipated to the experiment, for his company and for having been (exaggeratedly) optimistic even if things were getting worse (and also for the picture of the group). I would like also to thank people who I met during my week at ESRF for trasmitting me their passion for science.

There are no words to express my gratitude to my family that supported me throughout all my life, especially during the last years. A particular thanks to my grandparents and to Monica. I would like also to thank all my friends, the backbone of my life, and also *you*, that have supported, but more probably have put up with me during all these years. I owe to all of you what I am now and what I am able to do.

Visit at the “Fort de La Bastille" during experiment at ESRF. From the left, Mohamed, myself and Emilie. Unfortunately Marco is not present, but Mohamed later added him.